

**UNIWERSYTET JAGIELŁOŃSKI  
W KRAKOWIE**

**WYDZIAŁ FIZYKI, ASTRONOMII  
I INFORMATYKI STOSOWANEJ**

Mateusz Kmiec  
Nr albumu: 1125351

**Feasibility Studies of CPT Violation  
Measurement in Flavour Oscillations of  
the Neutral D Meson**

**MASTER THESIS IN PHYSICS  
IN THE FRAMEWORK OF STUDIES IN MATHEMATICS AND  
NATURAL SCIENCES**

Supervised by:  
dr inż. Wojciech Krzemień  
Department of Experimental Particle Physics and Applications, UJ

Cracow 2020

**UNIWERSYTET JAGIELŁOŃSKI  
W KRAKOWIE**

**WYDZIAŁ FIZYKI, ASTRONOMII  
I INFORMATYKI STOSOWANEJ**

Mateusz Kmiec  
Nr albumu: 1125351

**Studia możliwości łamania symetrii CPT  
w oscylacjach neutralnego mezonu  
zapachowego D**

**PRACA MAGISTERSKA Z FIZYKI  
NA KIERUNKU STUDIA MATEMATYCZNO-PRZYRODNICZE**

Praca wykonana pod kierunkiem:  
dr inż. Wojciecha Krzemienia  
Zakład Doświadczalnej Fizyki Cząstek i jej Zastosowań, UJ

Kraków 2020

## Acknowledgements

I would like to express my deepest gratitude to all people without whom this thesis would not have been completed. I am deeply indebted to my supervisor dr inż. Wojciech Krzemień for his invaluable guidance, unwavering support, and above all patience that cannot be underestimated. I would like to extend my sincere thanks to dr Adam Szabelski for his incredible dedication, valuable remarks and countless hours spent for discussion of results.

## Abstract

The main objective of this thesis was to perform feasibility studies of the CPT violation (CPTV) measurement in the system of the neutral  $D$  meson. CPT symmetry is one of the fundamental symmetries of the Standard Model (SM). The measurement of CPTV would mean that there exists physics beyond the SM. Studies of flavour oscillations of neutral mesons are a sensitive method facilitating precision tests of CPTV. My goal was to probe the level of sensitivity of testing CPTV in the system of the neutral  $D$  meson. For this purpose, I created a Monte Carlo (MC) generator of neutral meson decays, where CPTV was controlled by a complex phenomenological parameter  $z$ . The MC generator was used to simulate the CPT violation effect at the level of  $z = 0.1$  for an ensemble of 100 pseudo-experiments. Each experiment consisted of  $N = 6.5 \cdot 10^7$  of MC generated events corresponding to the number of  $D^0 \rightarrow K^+ \pi^-$  decays collected by the LHCb (2011-2012). For such statistics, the CPT violation effect would be seen at seven standard deviations level. This can be contrasted with the best experimental limit for the parameter  $z$  of order  $O(1)$  provided by the FOCUS collaboration.

**Keywords:** *neutral mesons, CPT, discrete symmetries, LHCb, meson oscillations*

## Streszczenie

Głównym celem tej pracy były badania możliwości pomiaru łamania CPT w oscylacjach neutralnego mezonu  $D$ . Symetria CPT jest zachowana w Modelu Standardowym cząstek elementarnych. Obserwacja łamania CPT oznaczałaby, że istnieje fizyka z poza MS. Pomiary oscylacji neutralnych mezonów zapachowych mogą być wykorzystywane jako precyzyjna metoda pozwalająca na testowanie łamania CPT. Moim celem było wyznaczenie poziomu czułości na badanie łamania CPT w układzie neutralnego mezonu  $D$ . W tym celu stworzyłem generator Monte Carlo (MC) rozpadów neutralnych mezonów, gdzie łamanie CPT było kontrolowane przez zespółony parametr  $z$ . Stworzony przeze mnie generator wykorzystałem do symulacji efektu CPT dla  $z = 0.1$  dla zestawu 100 pseudo-experymentów. Każdy pseudo-experryment zawierał  $N = 6.5 \cdot 10^7$  rozpadów wygenerowanych w generatorze MC, gdzie  $N$  odpowiada liczbie rozpadów z danych eksperimentalnych dla kanału  $D^0 \rightarrow K^+ \pi^-$  w eksperymencie LHCb (2011-2012). Dla takiej statystyki, efekt łamania CPT byłby widoczny na poziomie siedmiu odchyleń standardowych. Wynik ten można porównać z najlepszym obecnie eksperimentalnym ograniczeniem na parametr  $z$  w sektorze powabnym rzędu  $O(1)$  wyznaczonym przez projekt FOCUS.

**Słowa kluczowe:** *neutralne mezony, CPT, symetrie dyskretne, LHCb, oscylacje mezonów*

# Contents

<b>1. Introduction</b>	4
<b>2. Theory</b>	6
2.1. Symmetries	6
2.1.1. Discrete symmetries	6
2.1.2. CP symmetry/ CPT symmetry	7
2.2. Neutral meson system	7
2.3. CPV/ CPTV paramterisation	8
2.4. Notation remarks	10
2.5. Classification of CP violating effects	10
2.6. Candle plots	12
<b>3. Generator of Neutral Meson Oscillations</b>	14
3.1. Monte Carlo generator of neutral meson oscillations	14
3.2. Time dependent decay rates of mesons	14
3.3. Frequency of oscillations	17
3.4. Asymmetry and sensitivity assessment	18
3.5. MC generator test	19
<b>4. Analysis of CPTV in <math>D^0</math> system</b>	26
4.1. The LHCb experiment	27
4.2. Time-acceptance function	28
4.3. Gaussian smearing	29
4.4. Simplified asymmetry	29
4.5. Sensitivity tests for $ z  \leq 0.1$ used for data generation	31
4.6. Sensitivity tests for $ z  \leq 0.8$ used for data generation	33
4.7. Sensitivity tests for $ z  = 0.1$ used for generation of $6.5 \cdot 10^7$ decays	35
<b>5. Summary</b>	37
<b>Bibliography</b>	39
<b>A. Appendix</b>	40

# 1. Introduction

Particle physics is concerned with the fundamental constituents of the Universe, the elementary particles and the interactions between them. The Standard Model of particle physics (SM) is the embodiment of our current understanding of the sub-atomic Universe [1]. The SM describes three out of four fundamental forces: electromagnetic, strong and weak (leaving gravity aside). It provides a unified picture where the interactions between particles (quarks and leptons) are themselves mediated by the exchange of particles called bosons. In particle physics, each kind of interaction is described by a Quantum Field Theory (QFT). Remarkably, this model successfully describes all current experimental data and therefore is often viewed as one of the greatest achievements of modern physics.

In particle physics, we distinguish three main discrete transformations represented by two unitary operators  $\hat{C}$ ,  $\hat{P}$  and one antiunitary operator  $\hat{T}$ . The first operator is the charge conjunction operator  $\hat{C}$ , which transforms particles into their respective antiparticles. The second one is the parity operator  $\hat{P}$ , which reverses the sign of all position vector components. Finally, there is the time-reversal operator which changes the direction of time. In order to mathematically describe more complex symmetries, we can compose these three symmetry operators obtaining  $\hat{CP}$  and  $\hat{CPT}$  symmetry operators.

One of the greatest mysteries of modern physics is the observed matter-antimatter imbalance in the Universe. At present, there is an overwhelming consensus among physicists that in order to explain this discrepancy, three conditions, originally formulated by Sergei Sakharov in the year 1967 [2] must be satisfied, namely there must have been baryon number violation, C and CP symmetry violation as well as the existence of interactions out of thermal equilibrium. Even though the SM includes the possibility of CP violation in the weak interactions of quarks and leptons it fails to explain the matter-antimatter asymmetry in the Universe and ultimately new sources of CP violation need to be identified. The realisation of this fact sparked interest in testing of discrete symmetries. Among symmetries being tested today, there is CPT symmetry, which is intrinsically assumed to hold in the SM. Up until now, there is no experimental evidence of CPT symmetry breaking.

In particle physics, each kind of interaction is described by a Quantum Field Theory (QFT). At this point, it is worth noting that according to the CPT theorem every QFT, formulated on the flat space-time, which respects locality, unitarity and Lorentz invariance is CPT invariant [3,

4, 5]. Consequently, should we observe CPT violation there would emerge new physics beyond the SM.

One of the most promising potential areas where physics beyond the SM might be found are studies of discrete symmetries in neutral-meson oscillations. In this thesis, I am testing the feasibility of CPT violation measurement in the system of the flavoured neutral meson  $D^0$ . Mesons are bound quark-antiquark pairs. Flavoured neutral mesons are defined as mesons with no electric charge and non-zero strangeness, charm or beauty content. The weak interactions mix neutral-mesons with their antiparticles leading to spontaneous transitions between meson and antimeson quantum states, which can serve as a sensitive interferometer facilitating precision testing of CPT invariance and research into other fundamental symmetries [6].

In neutral-meson interferometry, CPT violation is modelled using a phenomenological description of the meson time evolution. In the present work, I am using CPT parametrisation with three complex parameters ( $p, q, z$ ). Their relation to discrete symmetries conservation is discussed in detail in the 2nd chapter of this thesis. At this point, it suffices to say that  $z \neq 0$  induces CPT symmetry breaking, and that it is possible to extract the boundary of sensitivity for the magnitude of the CPTV effect in the phenomenological description of the neutral-meson system from the fit of parameter  $z$  [7].

The main goal of this thesis was to establish the level of sensitivity of testing CPTV in the LHCb experiment. Throughout my research work, I focused on flavour oscillations in the system of meson  $D^0$  in the framework for which the CPTV parameter  $z$  is a constant complex number, as opposed to the Standard Model Extension framework where  $z$  can depend on the meson flavour and must depend on the direction and magnitude of the meson 3-momentum and its energy [8]. In the first part of this thesis, I briefly discussed all of the basic concepts needed for a theoretical description of CPTV in neutral-meson oscillations. Subsequently, I enlisted all of the necessary formulas for the development of neutral-meson oscillations generator. Among these formulas, there were two decay probability densities derived based on the information provided in [7, 9]. The 3rd chapter contains the tests of the Monte Carlo (MC) simulations and the fitting procedure using the derived generator. The 4th chapter focuses on the sensitivity tests for a few different statistics and parameter  $z$  values used for data generation. I performed multiple pseudo-experiments in order to find the statistical distribution of the CPTV parameter fit errors in relation to the CPTV parameter values. At the very end of the thesis I included A.Appendix which contains plots that are less important for the understanding of the text. All key results are presented in the summary.

## 2. Theory

### 2.1. Symmetries

#### 2.1.1. Discrete symmetries

In physics, a symmetry of a physical system is the feature of this system (observed or intrinsic) which is invariant under a certain transformation. Symmetries are often divided into two groups, which are discrete and continuous symmetries. According to Noether's theorem [10], continuous symmetries are connected with invariance under continuous transformations of parameters of the physical system e.g. translations in space are linked to the momentum conservation principle. However important these symmetries are in physics they won't be discussed any further as they are out of the scope of this thesis. In particle physics, we distinguish three main discrete transformations, which are usually represented as matrix operators, namely  $\hat{C}$ -charge conjunction,  $\hat{P}$ -parity transformation (point reflection) and  $\hat{T}$ -time-reversal. The first operator is the charge conjunction operator which transforms particles into their respective antiparticles. The second one is called parity operator  $\hat{P}$ , which changes the sign of all of the position vector components. Finally, there is the time-reversal operator which reverses the order in time. The manner in which these operators act on quantum states can be expressed mathematically as:

$$\begin{aligned}\hat{C} |c, \vec{p}, t\rangle &= |\bar{c}, \vec{p}, t\rangle, \\ \hat{P} |c, \vec{p}, t\rangle &= |c, -\vec{p}, t\rangle, \\ \hat{T} |c, \vec{p}, t\rangle &= \langle c, \vec{p}, -t|,\end{aligned}\tag{2.1}$$

where  $c$  denotes all possible charges (electric charge, baryon number, lepton numbers, etc.),  $\vec{p}$  represents momentum and  $t$  is time.

The sign of a physical system being invariant under a chosen discrete transformation is that its operator commutes with the Hamiltonian of the system provided that this operator does not depend explicitly on time. This simple test of invariance under discrete transformations can be written as:

$$[\hat{O}, \hat{H}] = 0,\tag{2.2}$$

where  $\hat{O}$  is the operator corresponding to the given discrete symmetry i.e.  $\hat{C}$ ,  $\hat{P}$  or  $\hat{T}$  and their compositions.

### 2.1.2. CP symmetry/ CPT symmetry

CP and CPT symmetries are mathematically represented by the composition of the respective discrete symmetry operators. As I have stated in the introduction there are no traces of CPT violation in any of the particle physics experiments performed to date. The assumption of CPT conservation for a given physical system implies T violation whenever CP symmetry is broken.

## 2.2. Neutral meson system

Mesons are quark-antiquark systems, where quarks are bound together by strong interactions. In physics, we distinguish an interesting type of mesons called flavoured neutral mesons. They are neutrally charged and have a net non-zero strangeness, charm or beauty content. This kind of mesons can only be distinguished from their antiparticles by their flavour quantum number. For such mesons, spontaneous transitions between their matter and antimatter states can be observed. This phenomenon is called neutral meson oscillations.

The Hamiltonian that governs time evolution of a flavoured neutral meson system is a sum of the strong, electromagnetic and weak Hamiltonians:

$$H = H_{st} + H_{em} + H_{wk}. \quad (2.3)$$

In non-relativistic quantum mechanics the state of the system represented by ket  $|\Psi(t)\rangle$  obeys the Schrödinger equation:

$$i\hbar \frac{d}{dt} |\Psi(t)\rangle = H |\Psi(t)\rangle. \quad (2.4)$$

If we are interested in time intervals, which are much larger than the typical strong interaction scale, the ket of the neutral-meson system must obey the Schrödinger equation in a simplified Weisskopf–Wigner approximation (WWA) formalism [11]:

$$i\hbar \frac{d}{dt} |\Psi(t)\rangle = H_{eff} |\Psi(t)\rangle = \left( m - \frac{i\Gamma}{2} \right) |\Psi(t)\rangle, \quad (2.5)$$

where  $H_{eff}$  is the effective Hamiltonian while  $\Gamma$  and  $M$  are hermitian matrixes.  $\Gamma$  provides the exponential decay component and  $M$  is a mass term. In this approach, the weak interactions are considered to be a perturbation to the sum of a strong and electromagnetic Hamiltonians. The time evolution of the eigenstates of the strong interactions is evaluated up to the second-order in weak interactions. The effective Hamiltonian  $H_{eff}$  is chosen so as to give the same evolution in the leading order of the perturbation theory [9, 11, 12]. If we constraint our space of all possible

states to linear combinations of only two neutral meson flavour states  $|M^0\rangle$  and  $|\bar{M}^0\rangle$  such that:

$$|\Psi(t)\rangle = a(t)|M^0\rangle + b(t)|\bar{M}^0\rangle, \quad (2.6)$$

where  $|a(t)|^2$  and  $|b(t)|^2$  are probabilities of finding the meson system in one of the two flavour states, we will obtain  $H_{eff}$  in the form of 2x2 matrix: (2.7):

$$H_{eff} = \left[ \begin{pmatrix} M_{11} & M_{12} \\ M_{12}^* & M_{22} \end{pmatrix} - \frac{i}{2} \begin{pmatrix} \Gamma_{11} & \Gamma_{12} \\ \Gamma_{12}^* & \Gamma_{22} \end{pmatrix} \right]. \quad (2.7)$$

At this point, it is worth noting that  $H_{eff}$  is non-hermitian which is reflected in the fact that  $|a(t)|^2 + |b(t)|^2$  decreases with time. This observation translates into states evolving into space from outside of our  $M^0 - \bar{M}^0$  subspace.

In this formalism our particle's state can be expressed as:

$$|\Psi(t)\rangle = \begin{pmatrix} a(t) \\ b(t) \end{pmatrix} \quad (2.8)$$

Consequently equation (2.5) takes the form:

$$i\hbar \begin{pmatrix} \dot{a}(t) \\ \dot{b}(t) \end{pmatrix} = H_{eff} \begin{pmatrix} a(t) \\ b(t) \end{pmatrix} = \left[ \begin{pmatrix} M_{11} & M_{12} \\ M_{12}^* & M_{22} \end{pmatrix} - \frac{i}{2} \begin{pmatrix} \Gamma_{11} & \Gamma_{12} \\ \Gamma_{12}^* & \Gamma_{22} \end{pmatrix} \right] \begin{pmatrix} a(t) \\ b(t) \end{pmatrix}. \quad (2.9)$$

### 2.3. CPV/ CPTV paramterisation

It was shown in the previous section that the effective Hamiltonian of a neutral-meson system can be represented as a 2x2 matrix (2.7), providing the considered time intervals are much longer then the typical time scale of strong interactions. It can be demonstrated [7, 10] that if CPT symmetry is conserved then:  $(M_{11} - M_{22}) - \frac{i}{2}(\Gamma_{11} - \Gamma_{22}) = 0$ , which is to say that  $M_{11} = M_{22}$  and  $\Gamma_{11} = \Gamma_{22}$ . Similarly, we can show that  $\hat{T}$  symmetry conservation indicates:  $\frac{|H_{12}|}{|H_{21}|} \Leftrightarrow H_{12} = e^{2i\eta_{CP}} H_{21}$ , where  $\eta_{CP}$  is an unobservable phase. Finally, CP invariance implies that both of the aforementioned conditions are fulfilled.

We can express the eigenvectors of the effective Hamiltonian (mass states) in terms of the strong interaction eigenstates (flavour states) from the  $M^0 - \bar{M}^0$  subspace, which leads us to the following elegant phenomenological CP/CPT complex parametrisation  $(q, p, z)$  [9]:

$$\begin{aligned} |M_L\rangle &= p\sqrt{1-z}|M^0\rangle + q\sqrt{1+z}|\bar{M}^0\rangle, \\ |M_H\rangle &= p\sqrt{1+z}|M^0\rangle - q\sqrt{1-z}|\bar{M}^0\rangle. \end{aligned} \quad (2.10)$$

In this formalism T conservation yields  $\left| \frac{q}{p} \right| = 1$ . CPT invariance induces  $z = 0$  and  $CP$  requires that both of these conditions are fulfilled. Parameters  $(q, p, z)$  are complex and they can be expressed in terms of their phase and modulus:

$$\begin{aligned} z &= |z|e^{i\Theta_{zz}}, \\ p &= |p|e^{i\Theta_{pp}}, \\ q &= |q|e^{i\Theta_{qq}}. \end{aligned} \quad (2.11)$$

The natural boundaries for these parameters are  $0 \leq |p| \leq 1$ ,  $0 \leq |q| \leq 1$ ,  $0 \leq |z| \leq 1$ . In addition, the analysis of linear coefficients in (2.10) results in  $|p|^2 + |q|^2 = 1$  for  $z = 0$ . The eigenstates of the effective Hamiltonian ( $|M_H\rangle$ ,  $|M_L\rangle$ ) have well-defined masses  $m_{H,L}$  and decay widths  $\Gamma_{H,L}$ . There are two eigenvalues of the effective Hamiltonian dependent on  $m_{H,L}$  and  $\Gamma_{H,L}$ . These two complex eigenvalues satisfy:

$$H_{eff} |M_{H,L}\rangle = \lambda_{H,L} |M_{H,L}\rangle, \quad (2.12)$$

where  $\lambda_{H,L} = m_{H,L} - i\Gamma_{H,L}/2$ . Equation (2.13) allows us to write the formula for the time evolution of mass states:

$$|M_{H,L}(t)\rangle = e^{-im_{H,L}t-\Gamma_{H,L}t/2} |M_{H,L}(0)\rangle. \quad (2.13)$$

From (2.10) we can find  $|M^0\rangle$ ,  $|\bar{M}^0\rangle$  as functions of  $|M_H\rangle$  and  $|M_L\rangle$ :

$$\begin{aligned} |M^0\rangle &= \frac{1}{2p} \left( \sqrt{1-z} |M_L\rangle + \sqrt{1+z} |M_H\rangle \right), \\ |\bar{M}^0\rangle &= \frac{1}{2q} \left( \sqrt{1+z} |M_L\rangle - \sqrt{1-z} |M_H\rangle \right). \end{aligned} \quad (2.14)$$

We can now add time evolution (2.13) to (2.14) and express mass eigenstates in flavour base using (2.14) again, which yields:

$$\begin{aligned} |M^0(t)\rangle &= (g_+(t) + zg_-(t)) |M^0\rangle - \sqrt{1-z^2} \frac{q}{p} g_-(t) |\bar{M}^0\rangle, \\ |\bar{M}^0(t)\rangle &= (g_+(t) - zg_-(t)) |\bar{M}^0\rangle - \sqrt{1-z^2} \frac{p}{q} g_-(t) |M^0\rangle, \end{aligned} \quad (2.15)$$

where  $g_{\pm}(t) = \frac{1}{2} \{ e^{-im_H t - \Gamma_H t/2} \pm e^{-im_L t - \Gamma_L t/2} \}$ .

## 2.4. Notation remarks

We define decay amplitudes of a neutral meson  $M^0$  and its CP conjugate  $\bar{M}^0$  to a multi-particle final state  $f$  and its CP conjugate  $\bar{f}$  as:

$$\begin{aligned} A_f &= \langle f | H_{wk} | M^0 \rangle, \\ A_{\bar{f}} &= \langle \bar{f} | H_{wk} | M^0 \rangle, \\ \bar{A}_f &= \langle f | H_{wk} | \bar{M}^0 \rangle, \\ \bar{A}_{\bar{f}} &= \langle \bar{f} | H_{wk} | \bar{M}^0 \rangle, \end{aligned} \tag{2.16}$$

where  $H_{wk}$  is the Hamiltonian governing weak interactions.

These amplitudes are complex and can be expressed in terms of their modulus and complex phase:

$$\begin{aligned} A_f &= |A_f| e^{i\Theta_{af}}, \\ A_{\bar{f}} &= |A_{\bar{f}}| e^{i\Theta_{afb}}, \\ \bar{A}_f &= |\bar{A}_f| e^{i\Theta_{aff}}, \\ \bar{A}_{\bar{f}} &= |\bar{A}_{\bar{f}}| e^{i\Theta_{affb}}. \end{aligned} \tag{2.17}$$

## 2.5. Classification of CP violating effects

The CP violation (CPV) is included in the SM by the Cabibbo–Kobayashi–Maskawa (CKM) matrix formalism [13] and can occur in three different ways [10].

1. CPV in decay, which manifests itself in different decay rates for  $M^0 \rightarrow f$  and  $\bar{M}^0 \rightarrow \bar{f}$ :

$$\Gamma(M^0 \rightarrow f) \neq \Gamma(\bar{M}^0 \rightarrow \bar{f}) \tag{2.18}$$

This is satisfied when  $\left| \frac{\bar{A}_{\bar{f}}}{A_f} \right| \neq 1$ .

2. CPV in mixing, which occurs when the probability of oscillation from meson to antimeson is different than from antimeson to meson:

$$\Gamma(M^0 \rightarrow \bar{M}^0) \neq \Gamma(\bar{M}^0 \rightarrow M^0), \tag{2.19}$$

which is equivalent to  $\left| \frac{q}{p} \right| \neq 1$ .

3. CPV in interference between a decay with and without mixing. In such a case, there are two amplitudes that we need to take into account while calculating the transition rate for  $M^0 \rightarrow f$ , namely  $A(M^0 \rightarrow f)$  and  $A(M^0 \rightarrow \bar{M}^0)A(\bar{M}^0 \rightarrow f)$ . This form of CPV occurs when:

$$\arg(\lambda_f) + \arg(\lambda_{\bar{f}}) \neq 0, \quad (2.20)$$

where  $\lambda_f = \frac{q}{p} \frac{\bar{A}_f}{A_f}$ .

For final CP eigenstates equation (2.20) simplifies to:

$$\text{Im}(\lambda_{f_{CP}}) \neq 0. \quad (2.21)$$

It is worth mentioning that a similar classification can be introduced for CPTV effects. Naturally, due to CPT invariance of the SM, the experimental observation of one of these three effects for CPT would be a major breakthrough and a signal of the existence of physics beyond the SM.

## 2.6. Candle plots

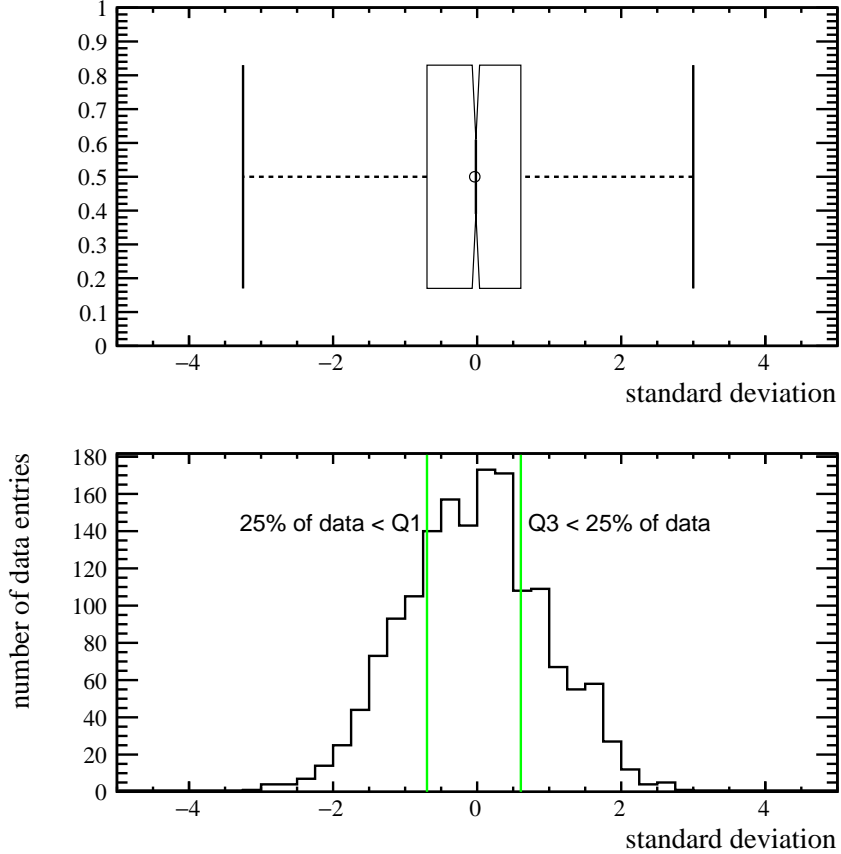


Figure 2.1 – Candle plot and the Gaussian histogram it was created from.

In the next two chapters I will frequently use candle plots for graphical representation of various distributions. Candle plots are a convenient way of description of data distributions invented in 1977 by John Tukey [14, 15], which can be represented with six markers.

1. The minimum value of the distribution.
2. The maximum value of the distribution.
3. The lower quartile  $Q1 > 25\%$  of data.
4. The upper quartile  $Q3 < 25\%$  of data.
5. Median.
6. Mean representing the arithmetic average of values of the distribution.

In Figure 2.1 the minimum and maximum values are represented by vertical whiskers ended with anchors. The box shows the position of interquartile range ( $Q1, Q3$ ), which contains 50% of data. The noches<sup>1</sup> represent the significance of the median  $1.57 \cdot \frac{IQR}{N}$ , where  $IQR$  is the size of the box and  $N$  is the number of all histogram entries. The median is drawn as a vertical line and the mean is represented as a circle. The definition of a candle is based on unbinned data. However ROOT Framework [15] used in this thesis, creates candles from binned data and

---

<sup>1</sup> narrowing of the box around the median

therefore too large values of bin widths might reflect poorly on the calculation of quartiles and medians.

In the further part of this thesis, I always specify the chosen markers below each candle plot. I also specify candle plot bin widths, which are so small that binning should have a negligible effect on the calculation of Q1, Q3, mean and median.

## 3. Generator of Neutral Meson Oscillations

### 3.1. Monte Carlo generator of neutral meson oscillations

One of the key elements of this thesis was the creation of a Monte Carlo generator (MC) of neutral-meson oscillations. Such a generator can be deployed to simulations of neutral meson mixing [7]. Its implementation requires knowledge of the time-dependent decay rates of both mesons and their associated antimesons, which gives us four possible decays within the specified decay mode ( $M^0 \rightarrow f$ ) <sup>1</sup>. Armed with this knowledge we can proceed with sampling a chosen number of events from each probability density distribution. Even though the implemented generator can be used to simulate all possible decays in a given decay mode, in the present work, I only considered decays for which both the initial and final states were of the same flavour. This assumption leaves us with just two possible decay probability distributions. It can be shown that for these particular decay modes we have high sensitivity for CPTV [7] and so it was natural to choose them. MC generated events can be used to create the asymmetry dataset by dividing the difference of data drawn from these distributions by their sum<sup>2</sup>. The whole procedure can be repeated many times creating multiple independent decay probability distributions and asymmetry datasets. In other words, we can use this procedure to perform many pseudo-experiments, which results can be treated as simulated neutral-meson oscillations.

### 3.2. Time dependent decay rates of mesons

The development of the neutral meson oscillations generator required derivation of the time-dependent decay rates of mesons. I considered two decay rates, namely the transition from the initial state  $|M^0\rangle$  to the final state  $|f\rangle$ , as well as, the transition from  $|\bar{M}^0\rangle$  to  $|\bar{f}\rangle$ . These transition rates can be obtained in the following way:

$$\frac{d\Gamma_{M^0 \rightarrow f}(t)}{dt} = |\langle f | H_{wk} | M^0(t) \rangle|^2, \quad (3.1)$$

$$\frac{d\Gamma_{\bar{M}^0 \rightarrow \bar{f}}(t)}{dt} = |\langle \bar{f} | H_{wk} | \bar{M}^0(t) \rangle|^2. \quad (3.2)$$

For the sake of simplicity let us introduce the following parameters:

---

<sup>1</sup> These four combinations are  $|M^0\rangle \rightarrow |f\rangle$ ,  $|\bar{M}^0\rangle \rightarrow |f\rangle$ ,  $|M^0\rangle \rightarrow |\bar{f}\rangle$  and  $|\bar{M}^0\rangle \rightarrow |\bar{f}\rangle$ .

<sup>2</sup> Bin by bin.

$$\begin{aligned}
\Delta m &= m_H - m_L, \\
\Delta \Gamma &= \Gamma_H - \Gamma_L, \\
\Gamma &= \frac{\Gamma_H + \Gamma_L}{2}.
\end{aligned} \tag{3.3}$$

Having introduced the aforementioned parameters we can expand formulas (3.1, 3.2) using (2.14, 2.16,, 3.3):

$$\begin{aligned}
\frac{d\Gamma_{M^0 \rightarrow f}(t)}{dt} &= \frac{\bar{A}_f^2 q^2 (|z|^2 - 1) e^{-\Gamma t} (\cos(\Delta m t) - \cosh(\frac{\Delta \Gamma t}{2}))}{2p^2} \\
&+ \frac{1}{2} A_f^2 e^{-\Gamma t} [(|z|^2 + 1) \cosh\left(\frac{\Delta \Gamma t}{2}\right) + (|z|^2 - 1) \cos(\Delta m t) \\
&- 2|z| \sinh\left(\frac{\Delta \Gamma t}{2}\right) \cos(\Theta_{zz}) \\
&+ 2|z| \sin(\Delta m t) \sin(\Theta_{zz})] \\
&+ \frac{q}{2p} 2A_f \bar{A}_f \sqrt{1 - |z|^2} e^{\frac{\Delta \Gamma t}{2} - \frac{1}{2}t(2\Gamma + \Delta \Gamma)} \sin(\Delta m t) \sin(\Theta_{af} - \Theta_{afb} + \Theta_{pp} - \Theta_{qq}) \\
&+ \frac{q}{2p} A_f \bar{A}_f \sqrt{1 - |z|^2} (1 - e^{\Delta \Gamma t}) e^{-\frac{1}{2}t(2\Gamma + \Delta \Gamma)} \cos(\Theta_{af} - \Theta_{afb} + \Theta_{pp} - \Theta_{qq}) \\
&- \frac{q}{2p} A_f \bar{A}_f z \sqrt{1 - |z|^2} e^{-\frac{1}{2}t(2\Gamma + \Delta \Gamma)} \left(e^{\Delta \Gamma t} - 2e^{\frac{\Delta \Gamma t}{2}} \cos(\Delta m t) + 1\right) \cos(\Theta_{af} - \Theta_{afb} + \Theta_{pp} - \Theta_{qq} + \Theta_{zz}). 
\end{aligned} \tag{3.4}$$

$$\begin{aligned}
\frac{d\Gamma_{\bar{M}^0 \rightarrow \bar{f}}(t)}{dt} &= \frac{A_{\bar{f}}^2 p^2 (|z|^2 - 1) e^{-\Gamma t} (\cos(\Delta m t) - \cosh(\frac{\Delta \Gamma t}{2}))}{2q^2} \\
&+ \frac{1}{2} \bar{A}_{\bar{f}}^2 e^{-\Gamma t} [(|z|^2 + 1) \cosh\left(\frac{\Delta \Gamma t}{2}\right) + (|z|^2 - 1) \cos(\Delta m t) \\
&+ 2|z| \sinh\left(\frac{\Delta \Gamma t}{2}\right) \cos(\Theta_{zz}) \\
&- 2|z| \sin(\Delta m t) \sin(\Theta_{zz})] \\
&+ \frac{p}{2q} 2A_{\bar{f}} \bar{A}_{\bar{f}} \sqrt{1 - |z|^2} e^{\frac{\Delta \Gamma t}{2} - \frac{1}{2}t(2\Gamma + \Delta \Gamma)} \sin(\Delta m t) \sin(\Theta_{aff} - \Theta_{affb} + \Theta_{pp} - \Theta_{qq}) \\
&+ \frac{p}{2q} A_{\bar{f}} \bar{A}_{\bar{f}} \sqrt{1 - |z|^2} (1 - e^{\Delta \Gamma t}) e^{-\frac{1}{2}t(2\Gamma + \Delta \Gamma)} \cos(\Theta_{aff} - \Theta_{affb} + \Theta_{pp} - \Theta_{qq}) \\
&- \frac{p}{2q} A_{\bar{f}} \bar{A}_{\bar{f}} |z| \sqrt{1 - |z|^2} e^{-\frac{1}{2}t(2\Gamma + \Delta \Gamma)} \left(e^{\Delta \Gamma t} - 2e^{\frac{\Delta \Gamma t}{2}} \cos(\Delta m t) + 1\right) \cos(\Theta_{aff} - \theta_{affb} + \Theta_{pp} - \Theta_{qq} + \Theta_{zz}). 
\end{aligned} \tag{3.5}$$

Where in accordance to the previous chapter  $\Theta_{pp}$ ,  $\Theta_{qq}$ ,  $\Theta_{zz}$  are arguments of complex  $(p, q, z)$  parameters (2.11). Similarly, phases  $\Theta_{af}$ ,  $\Theta_{afb}$ ,  $\Theta_{aff}$ ,  $\Theta_{affb}$  can be thought of as transition amplitude phases (2.17).

Subsequently, I compared the two aforementioned distributions (3.4, 3.5) with their simplified forms present in literature, so as to show that they were correctly derived.

Transition rates from (3.1, 3.2) can be written in a simplified form [7]. One of the formulas presented in [7] was derived with the assumption that CPT is violated ( $z \neq 0$ ) and that the direct transitions between states of different flavours are forbidden  $\bar{A}_f = A_{\bar{f}} = 0$ . In such a case probability densities (3.4, 3.5) tend to the following distributions:

$$\begin{aligned} \frac{d\Gamma_{M^0 \rightarrow f}(t)}{e^{-\Gamma t} dt} &= |< f | \mathcal{H}_{wk} | M^0(t) >|^2 = \\ &\frac{1}{2} A_f^2 [(1 + |z|^2) \cosh \left( \frac{\Delta\Gamma}{2} t \right) + (1 - |z|^2) \cos (\Delta m t)] \\ &+ 2 \operatorname{Re} \left\{ z \sinh \left( \frac{\Delta\Gamma}{2} t \right) \right\} - 2 \operatorname{Im} \{ z \sin (\Delta m t) \}. \end{aligned} \quad (3.6)$$

$$\begin{aligned} \frac{d\Gamma_{\bar{M}^0 \rightarrow \bar{f}}(t)}{e^{-\Gamma t} dt} &= |< \bar{f} | \mathcal{H}_{wk} | \bar{M}^0(t) >|^2 = \\ &\frac{1}{2} \bar{A}_{\bar{f}}^2 [(1 + |z|^2) \cosh \left( \frac{\Delta\Gamma}{2} t \right) + (1 - |z|^2) \cos (\Delta m t)] \\ &+ 2 \operatorname{Re} \left\{ z \sinh \left( \frac{\Delta\Gamma}{2} t \right) \right\} - 2 \operatorname{Im} \{ z \sin (\Delta m t) \}. \end{aligned} \quad (3.7)$$

They are consistent with the results presented in [7].

If we allow for CPT invariance and impose  $z = 0$ , it can be demonstrated that equations (3.1, 3.2) take the form:

$$\begin{aligned} \frac{d\Gamma_{M^0 \rightarrow f}(t)}{e^{-\Gamma t} dt} &= |< f | \mathcal{H}_{wk} | M^0(t) >|^2 = \\ &\left( |A_f|^2 - \left| \frac{q}{p} \bar{A}_f \right|^2 \right) \cos \left( \frac{\Delta m}{2} t \right) + \\ &\left( |A_f|^2 + \left| \frac{q}{p} \bar{A}_f \right|^2 \right) \cosh (\Delta \Gamma t) \\ &+ 2 \operatorname{Re} \left[ \left( \frac{q}{p} \right) A_f^* \bar{A}_f \right] \sinh \left( \frac{\Delta\Gamma}{2} t \right) - 2 \operatorname{Im} \left[ \frac{q}{p} A_f^* \bar{A}_f \right] \sin (\Delta m t), \end{aligned} \quad (3.8)$$

$$\begin{aligned}
\frac{d\Gamma_{\bar{M}^0 \rightarrow \bar{f}}(t)}{e^{-\Gamma t} dt} &= |<\bar{f}|\mathcal{H}_{wk}|\bar{M}^0(t)>|^2 = \\
&\left(|A_{\bar{f}}|^2 - \left|\frac{p}{q}\bar{A}_{\bar{f}}\right|^2\right) \cos\left(\frac{\Delta m}{2}t\right) + \\
&\left(|A_{\bar{f}}|^2 + \left|\frac{p}{q}\bar{A}_{\bar{f}}\right|^2\right) \cosh\left(\frac{\Delta\Gamma}{2}t\right) \\
&+ 2\operatorname{Re}\left[\left(\frac{p}{q}\right)\bar{A}_{\bar{f}}^* A_{\bar{f}}\right] \sinh\left(\frac{\Delta\Gamma}{2}t\right) - 2\operatorname{Im}\left[\frac{p}{q}\bar{A}_{\bar{f}}^* A_{\bar{f}}\right] \sin(\Delta mt),
\end{aligned} \tag{3.9}$$

which is consistent with the results presented in [9].

### 3.3. Frequency of oscillations

We can use (3.4) to calculate probability densities of decay  $\frac{d\Gamma(M^0 \rightarrow M^0)}{dt}$  and  $\frac{d\Gamma(M^0 \rightarrow \bar{M}^0)}{dt}$  (see Figure 3.2). If set  $z = 0$  (CPT invariance) and exclude all non-direct transitions e.g.  $(M^0 \rightarrow \bar{M}^0 \rightarrow M^0)$  we will end up with formulas presented in Figure 3.10. In this simplified form we can easily show that parameter  $\Delta m$  controls frequency of oscillations, which are modified by  $\cosh\left(\frac{\Delta\Gamma}{2}t\right)$  dependent on  $\Delta\Gamma$ .

$$\begin{aligned}
\frac{d\Gamma(M^0 \rightarrow M^0)}{dt} &\sim e^{-\Gamma t} \left[ \cosh\left(\frac{\Delta\Gamma}{2}t\right) + \cos(\Delta mt) \right] = I_1(t) \\
\frac{d\Gamma(M^0 \rightarrow \bar{M}^0)}{dt} &\sim e^{-\Gamma t} \left| \frac{q}{p} \right|^2 \left[ \cosh\left(\frac{\Delta\Gamma}{2}t\right) - \cos(\Delta mt) \right] = I_2(t)
\end{aligned} \tag{3.10}$$

At times, it is convenient to replace  $\Delta m$  and  $\Gamma$  in the formula above by  $x = \frac{\Delta m}{\Gamma}$ ,  $y = \frac{\Delta\Gamma}{2\Gamma}$ . If we look at Table 3.1 and the frequency of oscillations of flavoured neutral mesons in Figure 3.1, we shall see that the higher the value of modulus  $|x|$  the greater the number of oscillations per unit time. The obtained intensity plots differ significantly depending on the neutral meson family. The fastest oscillations can be observed for  $B_s^0$ , which on average changes flavour 25 times in a lifetime.

	$B_s^0$	$B^0$	$D^0$	$K^0$
$x$	25.194	0.773	0.006	-0.946
$y$	0.046	0.005	0.008	0.997

Table 3.1 –  $x, y$  calculated based on Particle Data Group data [16].

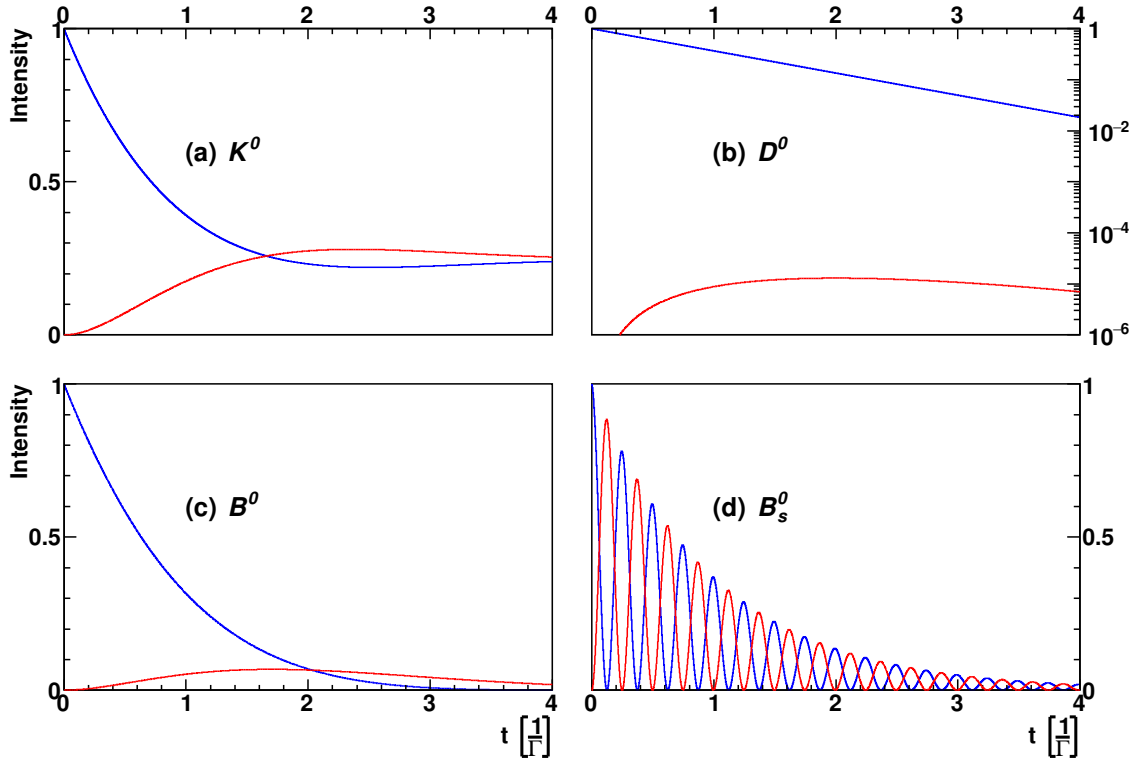


Figure 3.1 – Intensity corresponds to the values of  $I_1(t)$ ,  $I_2(t)$  from (3.10). Blue line corresponds to  $I_1(t)$  while red line corresponds to  $I_2(t)$ . In these plots I assume no CPV in mixing  $\left| \frac{q}{p} \right| = 1$ .

### 3.4. Asymmetry and sensitivity assessment

Using the model with CPTV parameter  $z$  we can generate two sets of  $N$  decays<sup>3</sup> corresponding to  $N$  meson and  $N$  to antimeson events. Next, we can construct the time-dependent asymmetry by dividing the difference of  $N$  events drawn from  $\frac{d\Gamma_{M^0 \rightarrow f}}{dt} \left( N \frac{d\Gamma_{M^0 \rightarrow f}}{dt} \right)$  and  $\frac{d\Gamma_{\bar{M}^0 \rightarrow \bar{f}}}{dt} \left( N \frac{d\Gamma_{\bar{M}^0 \rightarrow \bar{f}}}{dt} \right)$  by their sum (3.11).

$$\text{assymetry dataset}(t) = \frac{\frac{d\Gamma_{\bar{M}^0 \rightarrow \bar{f}}}{dt}(t) - \frac{d\Gamma_{M^0 \rightarrow f}}{dt}(t)}{\frac{d\Gamma_{\bar{M}^0 \rightarrow \bar{f}}}{dt}(t) + \frac{d\Gamma_{M^0 \rightarrow f}}{dt}(t)}, \quad (3.11)$$

Fitting our asymmetry model (3.12) to the newly created asymmetry dataset enables us to extract the value of the CPTV parameter  $z$  to determine its error.

$$A_{CPT}(t) = \frac{\frac{d\Gamma_{\bar{M}^0 \rightarrow \bar{f}}(t)}{dt} - \frac{d\Gamma_{M^0 \rightarrow f}(t)}{dt}}{\frac{d\Gamma_{\bar{M}^0 \rightarrow \bar{f}}(t)}{dt} + \frac{d\Gamma_{M^0 \rightarrow f}(t)}{dt}} + C, \quad (3.12)$$

where  $C$  is a real normalisation constant.

The error distribution over the ensemble of pseudo-experiments can be used to assess the sensitivity to CPTV of the fitting method.

---

<sup>3</sup> In this thesis, I used  $N \in \{10^6, 10^5, 1.8 \cdot 10^4, 1.8 \cdot 10^5, 6.5 \cdot 10^7\}$  statistics.

### 3.5. MC generator test

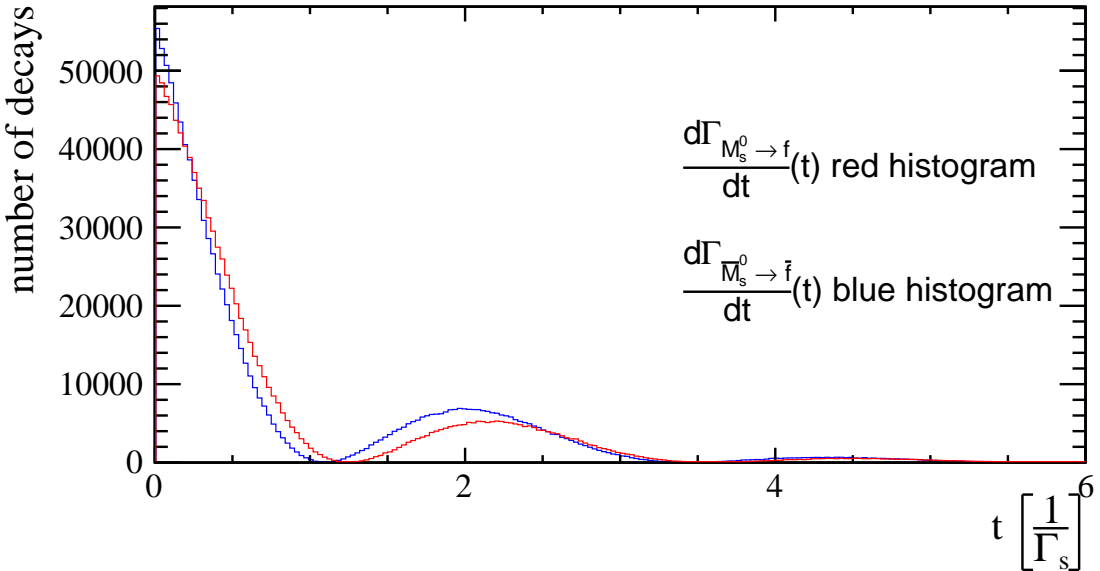


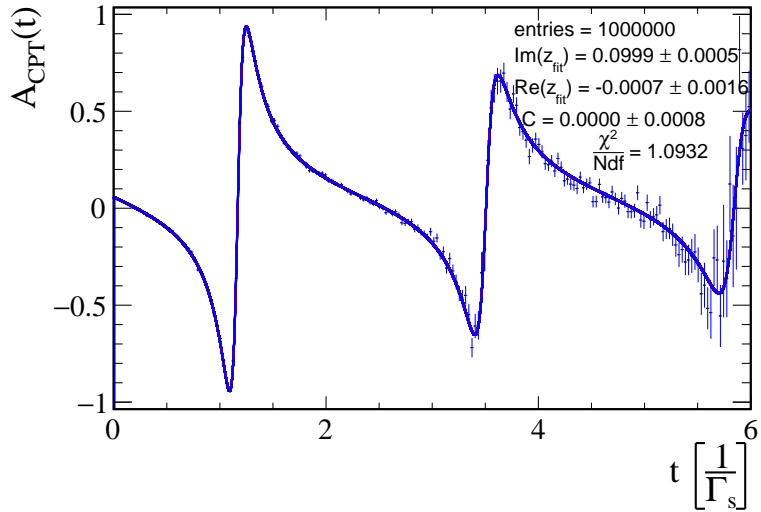
Figure 3.2 – Exemplary histograms of data from,  $\frac{d\Gamma(M_s^0 \rightarrow f)}{dt}$  and  $\frac{d\Gamma(M_s^0 \rightarrow \bar{f})}{dt}$  distributions. Bin widths are set to 0.03.

In order to demonstrate that my MC generator of neutral meson oscillations works properly, I decided to fit (3.12) to the asymmetry dataset created using this generator. Asymmetry dataset was created for  $\frac{d\Gamma(M_s^0 \rightarrow f)}{dt}$  and  $\frac{d\Gamma(M_s^0 \rightarrow \bar{f})}{dt}$  (see Figure.3.2), where  $M_s^0$  was a fictitious neutral meson with average decay width identical to that of meson  $B_s^0$  and mass difference  $\Delta m_s$  which amounts to 10% of  $B_s^0$  mass difference (3.3). The fitting procedure was performed for each of the 100 MC generated asymmetry datasets. The decision to take only a fraction of  $B_s^0$  mass difference was an attempt to reduce the number of oscillations (see Figure.3.1) and bolster the fitting algorithm’s efficiency. In addition, I only allow for the flavour-specific transitions, which means that there are no direct transitions to states of the opposite flavour.

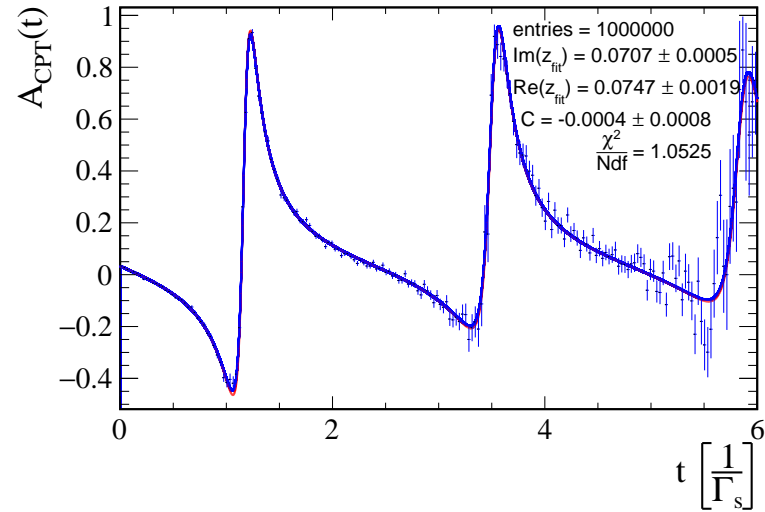
As far as the CPTV parameter is concerned, in the present chapter, I considered nine possible values of its argument  $\Theta_{zz}$  and four values of its modulus  $|z|$ . All of the chosen parameters can be found in (3.13). At this point, it is worth noting that the fit of parameter  $z$  was realised by fitting its real and imaginary parts,  $(\text{Re}(z))$  and  $(\text{Im}(z))$  instead of fitting  $|z|$  and  $\Theta_{zz}$ ). Another fitted parameter was the real constant  $C$ . All of the non-fit parameters were fixed at values provided in (3.13). When dealing with the fit parameters I specified their starting values, which were also included in (3.13).

$$\left\{ \begin{array}{l} \Delta m_s = 2.6843 \Gamma_s, \\ \Delta \Gamma_s = 0.1238 \Gamma_s, \\ |z| \in \{0.1, 0.01, 0.05, 0.001\}, \\ \Theta_{zz} = \{0, \frac{\pi}{8}, \frac{\pi}{4}, \frac{\pi}{2}, \frac{7\pi}{10}, \frac{9\pi}{10}, \frac{5\pi}{4}, \frac{8\pi}{5}, \frac{9\pi}{5}\} \\ \left| \frac{q}{p} \right| = 1, \\ C = 0, \\ A_f = \bar{A}_{\bar{f}} = 1, \\ A_{\bar{f}} = \bar{A}_f = 0. \text{ (flavour-specific)} \end{array} \right. . \quad (3.13)$$

For the sake of legibility, I decided to plot only two fits of (3.12) to the asymmetry dataset. The presented fits were performed for datasets where parameters  $|z| = 0.1$ ,  $\Theta_{zz} = \frac{\pi}{2}$  ( $\text{Re}(z) = 0$ ,  $\text{Im}(z) = 0.1$ ) and  $|z| = 0.1$ ,  $\Theta_{zz} = \frac{\pi}{4}$  ( $\text{Re}(z) \approx 0.0707$ ,  $\text{Im}(z) \approx 0.0707$ ) were used for MC simulation. The two graphs contain one asymmetry dataset marked with blue points and error bars, as well as two plots each, the blue one and the red one. The former signifies fit to data and the latter represents (3.12) function plotted for the parameters corresponding to those of the probability density distributions (3.4, 3.5), from which asymmetry data were drawn. In this case, the red plot is hardly visible due to the fact that both plots are overlapping.



(a) Blue - fit, red - model,  
for  $|z| = 0.1$ ,  $\Theta_{zz} = \frac{\pi}{2}$  used for simulation,  
where bin width is set to 0.03.



(b) Blue - fit, red - model,  
for  $|z| = 0.1$ ,  $\Theta_{zz} = \frac{\pi}{4}$  used for simulation,  
where bin width is set to 0.03.

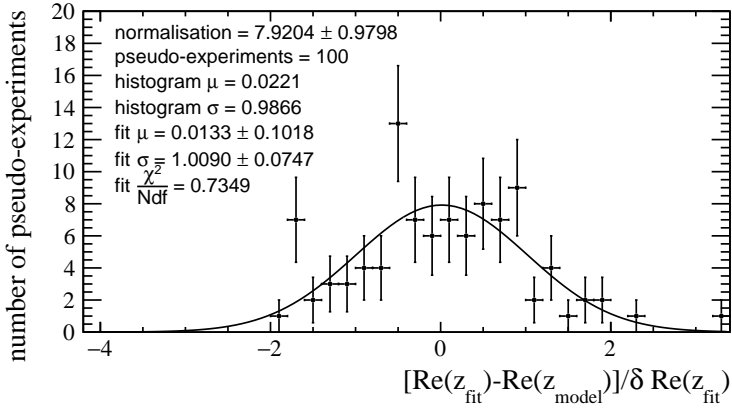
Figure 3.3 – Exemplary asymmetry fits. Fit results and the plotted models are overlapping and so not all of them are visible. Blue points with error bars represent the generated asymmetry dataset.

In order to examine, whether there are any systematic biases of the 100 fits of (3.12) to MC generated asymmetry datasets, I plotted the differences between the fitted parameter values  $\text{Im}(z_{\text{fit}})$ ,  $\text{Re}(z_{\text{fit}})$  and  $\text{Im}(z_{\text{model}})$ ,  $\text{Re}(z_{\text{model}})$ , which were presented in (Figure.3.14). They were calculated for  $z$  from (3.13) and used for the asymmetry datasets generation.

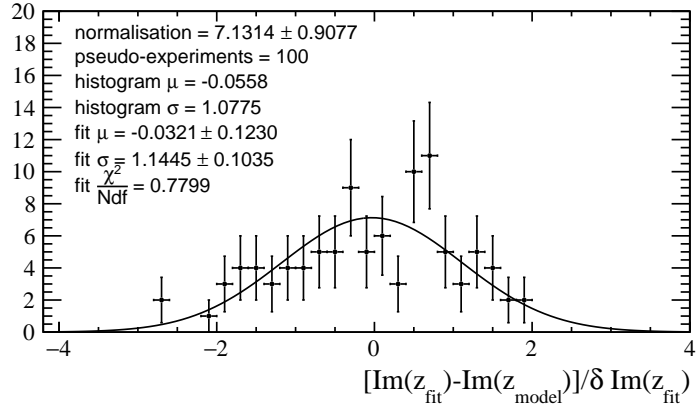
$$\begin{aligned}\text{Im}(z_{\text{model}}) &= |z| \sin(\Theta_{zz}) \\ \text{Re}(z_{\text{model}}) &= |z| \cos(\Theta_{zz}).\end{aligned}\tag{3.14}$$

We would expect that these differences divided by the respective fit errors are distributed according to the Gaussian distribution with standard deviation equal to unity. Histograms filled with such values are often called pull distributions. Examples of such plots for asymmetry MC simulation parameters  $|z| = 0.1$ ,  $\Theta_{zz} = \frac{\pi}{2}, \frac{\pi}{4}$  were presented in Figure.3.4. If we look at Figure.3.4 we shall see that all of the means obtained from both the fit of Gaussian distributions to histograms (labelled fit in Figure.3.4), as well as, the means acquired using `TH1::GetMean()`; ROOT function for pull histograms (labelled histogram in Figure.3.4) are consistent with zero to within one standard deviation  $\sigma$ . Which does not mean however that there is no fit bias. For Figure.3.4.d we observe that the pull histogram for  $\text{Re}(z)$  is not centred at zero but shifted in the positive direction of time axis. The size of this shift amounts to nearly 80% of the estimated Gaussian fit uncertainty. Figures.3.5.a, 3.5.b correspond to  $\chi^2$  distribution over the ensemble of 100 pseudo-experiments mentioned earlier. The fitted number of the degrees of freedom for Figure.3.5.a is identical to the real number of the degrees of freedom for each pseudo-experiment (which is 197). The distribution from Figure.3.5.b is also pretty close to the expected value of the degrees of freedom but differs from the expected value by 2.

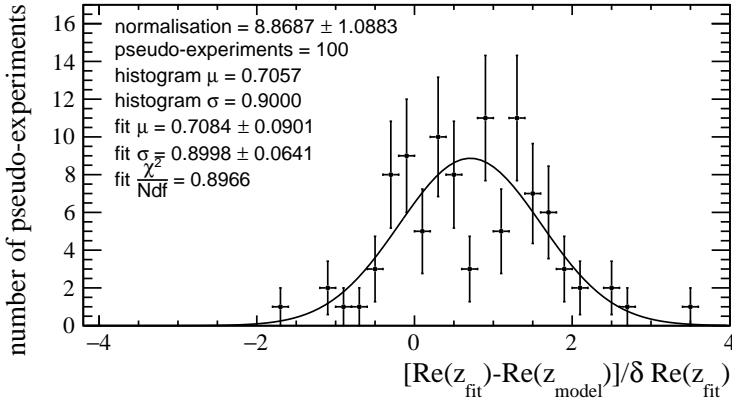
All of the remaining pull histograms for  $|z| = 0.1$  and the nine angles from (3.13) are presented in the form of a candle plot in Figure.3.6. The candle plot constructed for pull histograms of the constant parameter  $C$  can be found in A.Appendix (Figure.A.2).



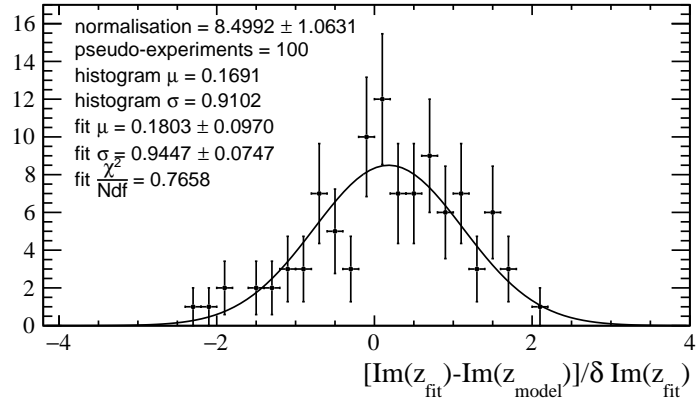
(a)  $\text{Re}(z)$  pull distribution histogram, data generated for  $|z| = 0.1, \Theta_{zz} = \frac{\pi}{2}$



(b)  $\text{Im}(z)$  pull distribution histogram, data generated for  $|z| = 0.1, \Theta_{zz} = \frac{\pi}{2}$

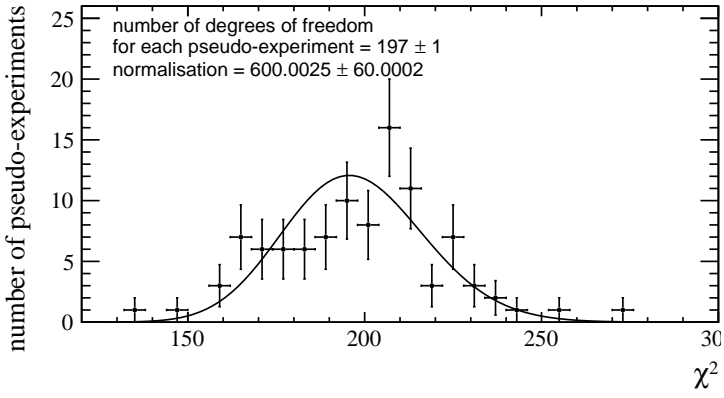


(c)  $\text{Re}(z)$  pull distribution histogram, data generated for  $|z| = 0.1, \Theta_{zz} = \frac{\pi}{4}$

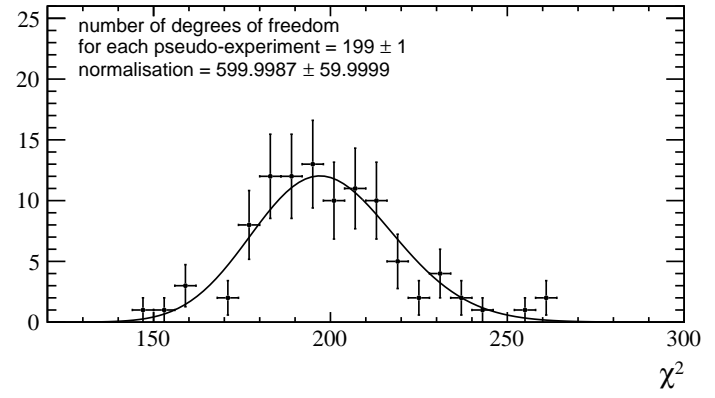


(d)  $\text{Im}(z)$  pull distribution histogram, data generated for  $|z| = 0.1, \Theta_{zz} = \frac{\pi}{4}$

Figure 3.4 – Pull histograms, data generated for  $10^6$  decays in each of 100 pseudo-experiments for (a, b, c, d). The CPT violation parameter was set to  $|z| = 0.1, \Theta_{zz} = \frac{\pi}{2}$  or  $\frac{\pi}{4}$  for data generation. Bin widths of the histograms are all set to 0.2.

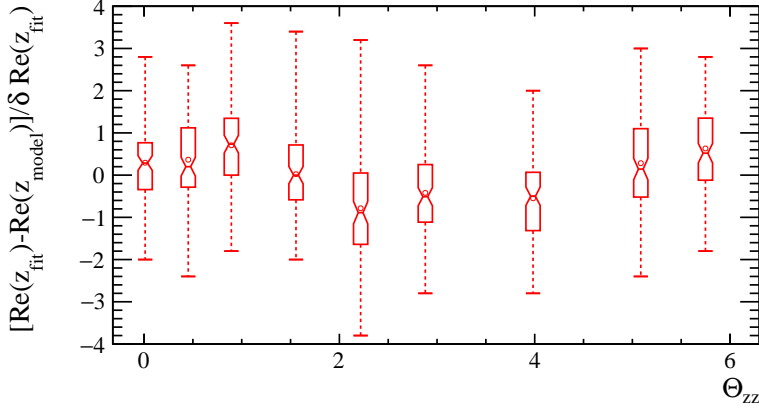


(a)  $\chi^2$  for MC generation parameters  $|z| = 0.1, \Theta_{zz} = \frac{\pi}{2}$ .

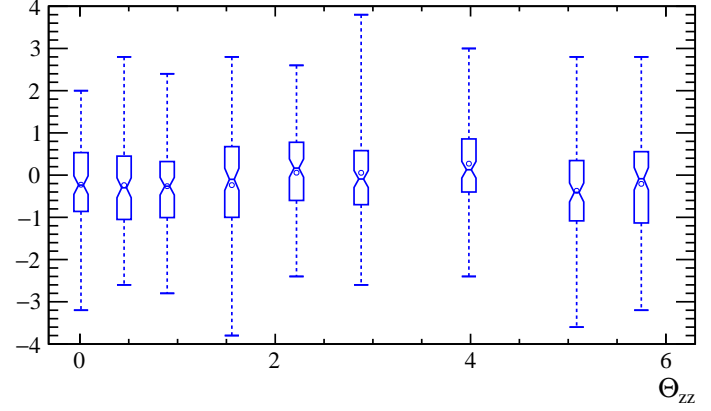


(b)  $\chi^2$  for MC generation parameters  $|z| = 0.1, \Theta_{zz} = \frac{\pi}{4}$ .

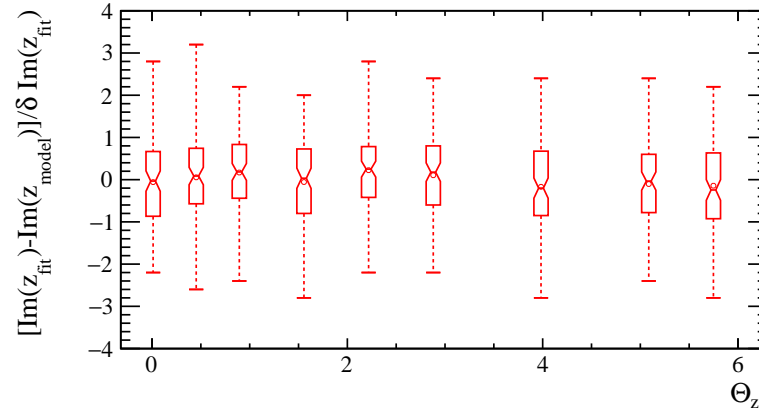
Figure 3.5 –  $\chi^2$  distribution of 100 fits of (3.12) to MC generated data. There were 200 bins in each pseudo-experiment and 3 parameters were fitted. The fitted number of degrees of freedom is close to the real number of degrees of freedom, which is 197. These two histograms were created for  $10^6$  decays in each of 100 pseudo-experiments. Bin widths of the histograms are both 0.2



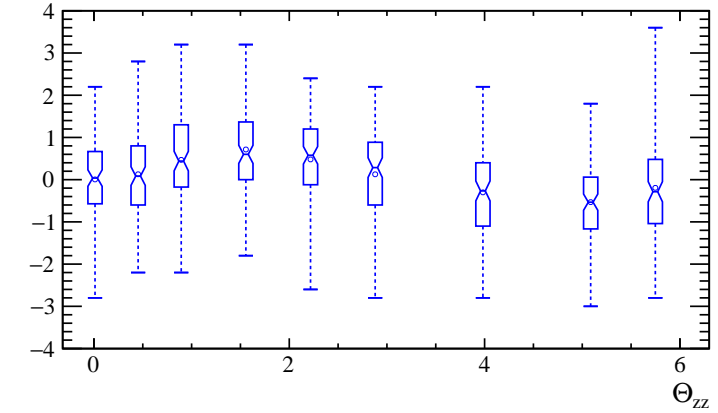
(a) Candle plot of  $\text{Re}(z)$  pull distributions  
(all six markers displayed).



(b) Candle plot of  $\text{Re}(z)$  pull distributions  
(all six markers displayed).

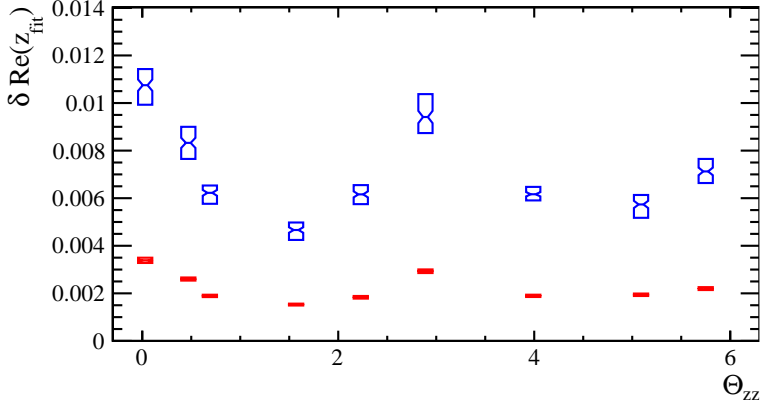


(c) Candle plot of  $\text{Im}(z)$  pull distributions  
(all six markers displayed).

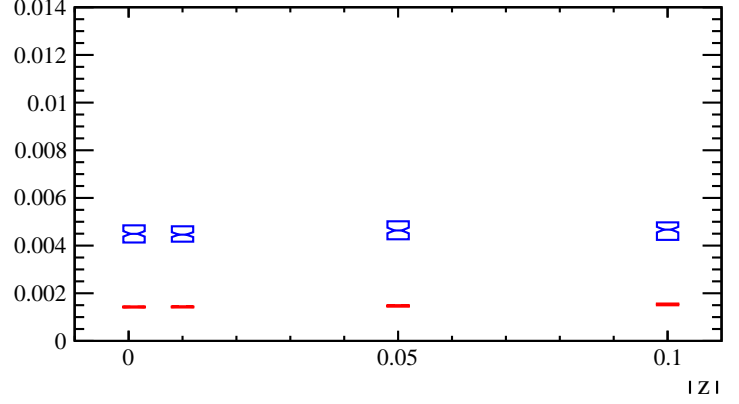


(d) Candle plot of  $\text{Im}(z)$  pull distributions  
(all six markers displayed).

Figure 3.6 –  $10^5$  decays in each pseudo-experiment blue (b,d),  $10^6$  decays in each pseudo-experiment red (a,c). There is 100 psuedo-experiments in each candle. Candle plot vertical bin widths  $10^{-6}$ . Data was generated for parameters  $|z| = 0.1$ ,  $\Theta_{zz} \in \{0, \frac{\pi}{8}, \frac{\pi}{4}, \frac{\pi}{2}, \frac{7\pi}{10}, \frac{9\pi}{10}, \frac{5\pi}{4}, \frac{8\pi}{5}, \frac{9\pi}{5}\}$ .

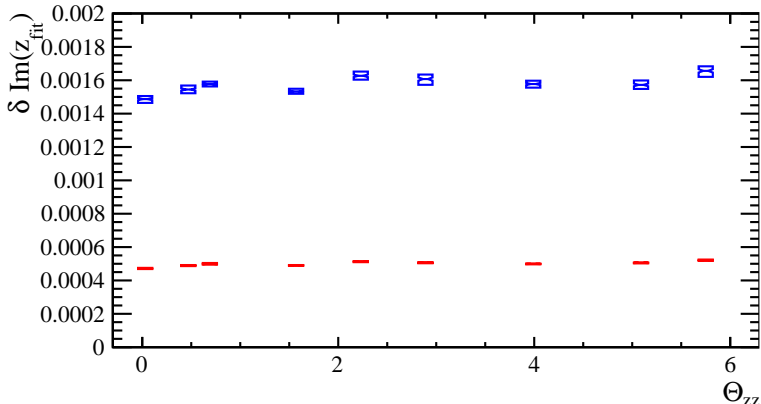


(a)  $|z| = 0.1, \Theta_{zz} \in \{0, \frac{\pi}{8}, \frac{\pi}{4}, \frac{\pi}{2}, \frac{7\pi}{10}, \frac{9\pi}{10}, \frac{5\pi}{4}, \frac{8\pi}{5}, \frac{9\pi}{5}\}$

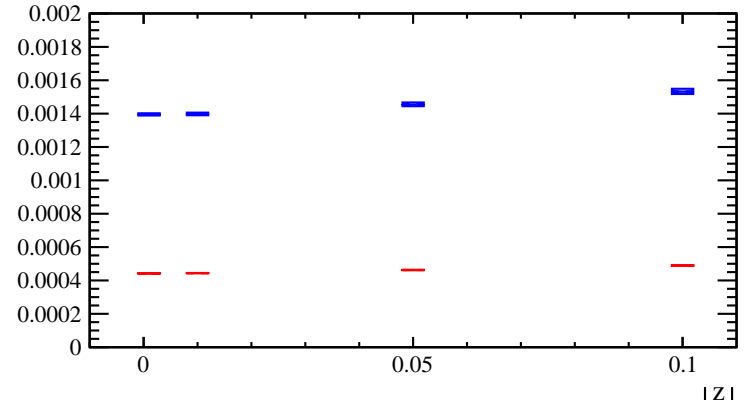


(b)  $|z| \in \{0.1, 0.05, 0.01, 0.001\}, \Theta_{zz} = \frac{\pi}{2}$

Figure 3.7 – Candle plots of  $\delta \text{Re}(z_{\text{fit}})$  distributions (boxes and medians displayed). 100 pseudo-experiments in each candle. (blue)  $10^5$  decays in each pseudo-experiment, (red)  $10^6$  decays in each pseudo-experiment. Data generated for parameter  $z$  values defined under each plot. Candle plot vertical bin widths  $10^{-6}$ . Some boxes are reduced to lines in this scale.



(a)  $|z| = 0.1, \Theta_{zz} \in \{0, \frac{\pi}{8}, \frac{\pi}{4}, \frac{\pi}{2}, \frac{7\pi}{10}, \frac{9\pi}{10}, \frac{5\pi}{4}, \frac{8\pi}{5}, \frac{9\pi}{5}\}$



(b)  $|z| \in \{0.1, 0.05, 0.01, 0.001\}, \Theta_{zz} = \frac{\pi}{2}$

Figure 3.8 – Candle plots of  $\delta \text{Im}(z_{\text{fit}})$  distributions (boxes and medians displayed). 100 psuedo-experiments in each candle. (blue)  $10^5$  decays in each pseudo-experiment, (red)  $10^6$  decays in each pseudo-experiment. Data generated for parameter  $z$  values defined under each plot. Candle plot vertical bin widths  $10^{-6}$ . Some boxes are reduced to lines in this scale.

By analysing the candle plot consisting of pull distributions represented by candles for each one of the nine arguments from (3.13), we shall quickly learn that all of their means and medians are located to within one standard deviation from zero. Unfortunately, some of them have a significant bias, which might have its source in high correlations between fit parameters (see Table.3.2).

Establishing the sensitivity of testing CPTV in neutral meson oscillations requires knowledge of the dependence between the value of the CPTV parameter and the average<sup>4</sup> value of 100 fit errors of parameter  $z$  to the MC generated asymmetry dataset. In this section, I presented studies of how the errors of the fitted real and imaginary parts ( $\delta \operatorname{Re}(z_{\text{fit}})$ ,  $\delta \operatorname{Im}(z_{\text{fit}})$ ) depend on the modulus and argument of  $z$  used to generate the analysed 100 pseudo-experiments.

If both median values of  $\delta \operatorname{Re}(z_{\text{fit}})$  and  $\delta \operatorname{Im}(z_{\text{fit}})$  distributions over 100 pseudo-experiments were invariant with respect to the change of  $z$  used for generation, the sensitivity of testing CPTV would depend only on the available statistics of decays. In this case, however,  $\delta \operatorname{Re}(z_{\text{fit}})$  and  $\delta \operatorname{Im}(z_{\text{fit}})$  are not independent of the choice of  $z$ . Luckily, we can easily observe (see Figures.3.7, 3.8) that for different  $\Theta_{zz}$  all error values are within a certain finite interval. As expected, the errors for  $10^6$  decays (see Figures.3.7, 3.8) are approximately  $\sqrt{10} \approx 3$  times smaller than their counterparts for ten times smaller statistics.

$\Theta_{zz}$	0	$\frac{\pi}{8}$	$\frac{\pi}{4}$	$\frac{\pi}{2}$	$\frac{7\pi}{10}$	$\frac{9\pi}{10}$	$\frac{5\pi}{4}$	$\frac{8\pi}{5}$	$\frac{9\pi}{5}$
$\operatorname{corr}(\operatorname{Re}(\mathbf{z}_{\text{fit}}), \operatorname{Im}(\mathbf{z}_{\text{fit}}))$	-0.10	0.26	0.31	-0.07	-0.35	-0.37	0.28	-0.28	-0.41
$\operatorname{corr}(\operatorname{Re}(\mathbf{z}_{\text{fit}}), \mathbf{C}_{\text{fit}})$	0.37	0.28	0.29	0.36	0.44	0.47	0.29	0.44	0.46
$\operatorname{corr}(\operatorname{Im}(\mathbf{z}_{\text{fit}}), \mathbf{C}_{\text{fit}})$	-0.41	-0.24	-0.14	-0.32	-0.33	-0.44	-0.16	-0.42	-0.38

Table 3.2 – This table represents the correlations between asymmetry fit parameters for various values of argument  $\Theta_{zz}$  of the CPTV parameter  $z$ .

---

<sup>4</sup> Average over 100 pseudo-experiments, mean or median. In this thesis, I am using medians which are a natural choice in the context of frequentist coverage

## 4. Analysis of CPTV in $D^0$ system

My goal was to measure the sensitivity of testing CPTV in the system of the neutral  $D$  meson. Flavoured neutral meson  $D^0$  is characterised by slow oscillations (see Figure 3.1) due to low mass difference  $\Delta m_{D^0}$  and average decay width  $\Delta\Gamma_{D^0}$ . The neutral meson  $D^0$  parameters taken from [16] were gathered in (4.1). Despite the fact that my generator allows for the analysis of all transitions regardless of their flavour, just as in the previous chapter, I restricted myself to the analysis of decays where direct transitions to the states of the opposite flavour were forbidden  $A_{\bar{f}} = \bar{A}_f = 0$  (flavour-specific), which are the modes with the highest sensitivity for CPTV. In this context, I repeated all of the steps from the 3rd chapter. However this time all of the fit correlations between  $\text{Im}(z)$  and  $\text{Re}(z)$  were close to unity. For this reason, I decided to fit only one  $z$  component each time. When parameter  $\text{Re}(z)$  was fixed then  $\text{Im}(z)$  and  $C$  were fitted and vice versa. As far as the model parameters are concerned, six arguments and four values of the modulus of  $z$  were considered (4.1). Another novelty in this chapter is the introduction of time-acceptance and Gaussian smearing to account for the detector performance and the uncertainties of the decay time measurement. Pull histograms for  $\text{Im}(z)$  and  $\text{Re}(z)$  distributions can be found in A.Appendix (Figures A.4, A.5, A.6, A.7). Interestingly, this time arithmetic averages and medians of pull distributions are consistent with zero to within 10% of the standard deviation<sup>1</sup>.

$$\left\{ \begin{array}{l} \Delta m_{D^0} = 0.0038 \Gamma_{D^0}, \\ \Delta\Gamma_{D^0} = 0.0129 \Gamma_{D^0}, \\ |z| \in \{0.1, 0.01, 0.05, 0\}, \\ \Theta_{zz} \in \{0, \frac{\pi}{8}, \frac{\pi}{4}, \frac{\pi}{2}, \frac{5\pi}{4}, \frac{9\pi}{5}\}, \\ \left| \frac{q}{p} \right| = 0.92, \\ C = 0, \\ A_f = \bar{A}_{\bar{f}} = 1, \\ A_{\bar{f}} = \bar{A}_f = 0. \text{ (flavour-specific)} \end{array} \right. . \quad (4.1)$$

---

<sup>1</sup> ROOT function TH1::GetStdDev(); [15]

## 4.1. The LHCb experiment

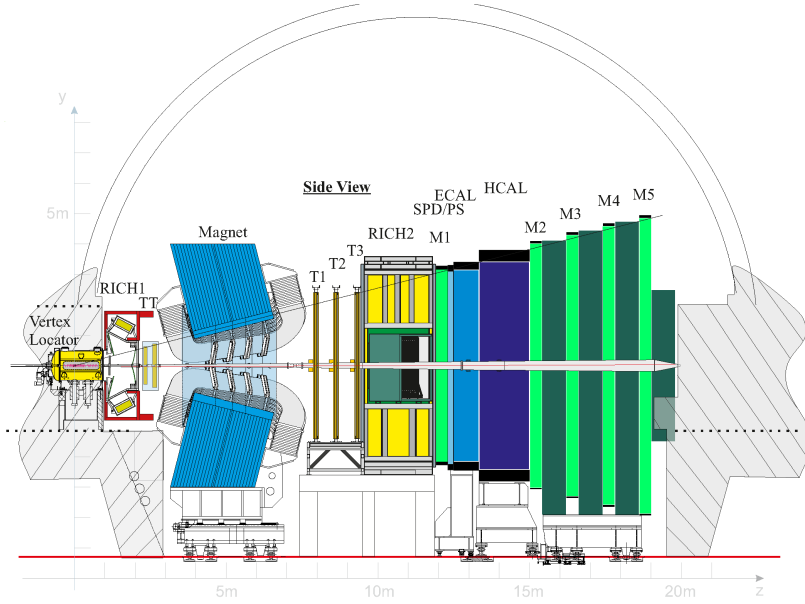


Figure 4.1 – LHCb detector, (ECAL, HCAL) - electromagnetic and hadronic calorimeters, (M1, M2, M3, M4) - muon detectors, RICH1, RICH2 Cherenkov detectors, (T1,T2,T3, TT)-silicon strip detectors [17].

The Large Hadron Collider (LHC), located at CERN in Geneva, accelerates protons, which collide with 7TeV, 8TeV and 13TeV energies, at the center of mass frame. The protons are moving inside underground tunnels in opposite directions. These tunnels contain ultra high vacuum and strong bending electromagnets used to guide the colliding beams [18]. The LHCb detector is located at one of the four points where beams of protons are smashed together, producing an array of different particles [18, 19]. The LHCb is a single-arm forward spectrometer covering the pseudorapidity range  $2 < \eta < 5$ , designed for the study of particles from the charm and beauty sectors [20]. The detector includes a tracking system (VELO) consisting of a silicon-strip vertex detector surrounding the proton-proton interaction region. Downstream from the vertex locator there is one of the two ring-imaging Cherenkov detectors (RICH1, RICH2). They are used to distinguish charged hadrons. Photons, electrons and hadrons are identified by a system of calorimeters, which consists of an electromagnetic and a hadronic calorimeter (ECAL, HCAL). Muons are identified by a system composed of alternating layers of iron and multiwire proportional chambers (M1, M2, M3, M4, M5). Downstream from RICH1, there is a silicon-strip (TT). Further down there is dipole magnet, with a bending power of about 4Tm, and three stations of silicon-strip detectors and straw drift tubes (T1, T2, T3).

In the present study, I tuned my generator so as to produce a similar dataset to that collected by the LHCb experiment during LHC’s Run 1 (2011-2012), at the centre-of-mass energies 7TeV and 8TeV corresponding to an integrated luminosity of  $3\text{fb}^{-1}$ . Between 2015 and 2018 there was another LHC Run (Run 2), with 13TeV energy at the centre of mass corresponding to an integrated luminosity of  $6\text{fb}^{-1}$ . The LHCb experiment collected the largest sample of data in the charm sector to date. High statistics<sup>2</sup> of data combined with excellent time resolution of about  $\sim 45\text{fs}$  [20] facilitates precise studies of time-dependent asymmetry.

## 4.2. Time-acceptance function

In order to account for technical time performance of the LHCb detector we may multiply probability density distributions (3.4, 3.5) by the time-acceptance function (see Figure 4.2), which represents the fraction of registered decays for a given decay time. In this thesis I am using the time-acceptance of the LHCb spectrometer derived for experimental data from  $D^0 \rightarrow K^-\pi^+$  decay mode LHCb (2011-2012), which is the most promising mode for the CPTV studies [7]. The time-acceptance function can be mathematically expressed as:

$$\text{acceptance}(t) = \begin{cases} \frac{(x-p_0)^{p_1}}{(1+p_2)\cdot(x-p_0)^{p_1}}, & t \geq 0.6 \\ 0, & t < 0.6 \end{cases}, \quad (4.2)$$

where we have the following parameter values<sup>3</sup>;  $p_0 = 0.6$ ,  $p_1 = 1.5$ ,  $p_2 = 2$ .

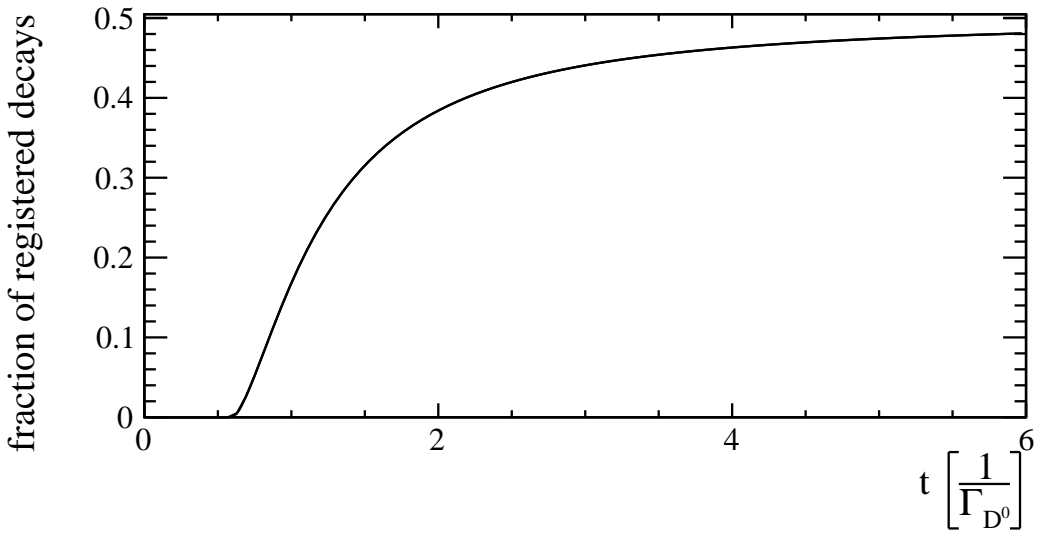


Figure 4.2 – Time-acceptance derived for experimental data from  $D^0 \rightarrow K^-\pi^+$  decay mode LHCb (2011-2012).

<sup>2</sup> The number of signal candidates from the combined Run 1 and 2 data are of order  $1.77 \cdot 10^8$ .

<sup>3</sup> Parameter values  $p_0, p_1, p_2$  private communication with dr inż. Wojciech Krzemień.

### 4.3. Gaussian smearing

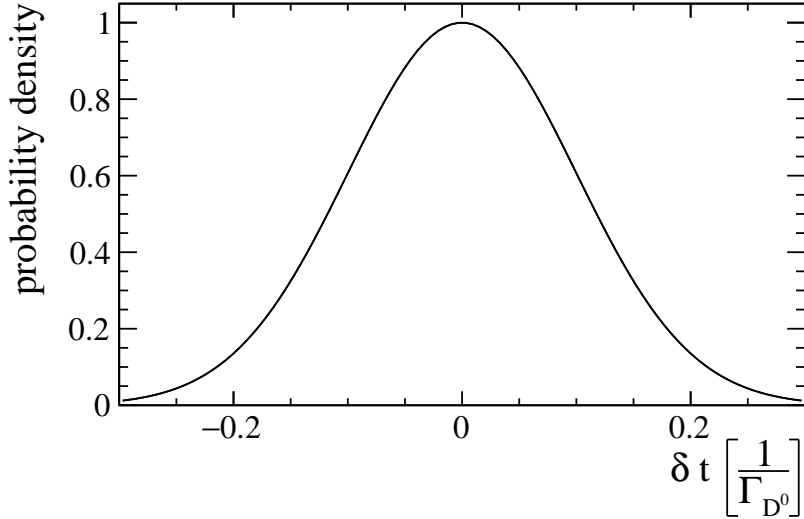


Figure 4.3 – Standard deviation  $\sigma = 1/\Gamma_{D^0}$ , which is equivalent to 45fs [20].

The effect of non-zero decay time measurement resolution 45fs, which corresponds to detector time resolution of  $D^0 \rightarrow K^- \pi^+$  measurement in LHCb [20], can be simulated by a numerical convolution of the probability density distributions, from which we draw data to construct asymmetry dataset with the Gaussian distribution presented in Figure 4.3.

### 4.4. Simplified asymmetry

If we choose (flavour-specific) final state  $A_{\bar{f}} = \bar{A}_f = 0$ . The asymmetry model (3.12) can be written in the form [21]:

$$A_{CPT}(t) = \frac{2 \operatorname{Re}(z) \left( \frac{\Delta \Gamma t}{2} \right) - 2 \operatorname{Im}(z) (\Delta m t)}{(1 + |z|^2) \left( \frac{\Delta \Gamma t}{2} \right) + (1 - |z|^2) (\Delta m t)} + C, \quad (4.3)$$

where  $C = \frac{|\bar{A}_f|^2 - |A_f|^2}{|\bar{A}_{\bar{f}}|^2 + |A_f|^2} = 0$  for parameters  $A_f = \bar{A}_{\bar{f}} = 1$  taken from (4.1).

For small  $x = \frac{\Delta m}{\Gamma} \ll 1$  and  $y = \frac{\Delta \Gamma}{2\Gamma} \ll 1$ , we can approximate the following functions to the

first term of the Taylor series expansion:

$$\begin{aligned}
\cosh\left(\frac{\Delta\Gamma t}{2}\right) &= \cosh(y) \approx 1, \\
\cos(\Delta mt) &= \cos(x) \approx 1, \\
\sinh\left(\frac{\Delta\Gamma t}{2}\right) &= \sinh(y) \approx \frac{\Delta\Gamma t}{2}, \\
\sinh\left(\frac{\Delta\Gamma t}{2}\right) &= \sinh(y) \approx \frac{\Delta\Gamma t}{2}, \\
\sin(\Delta mt) &= \sin(x) \approx \Delta mt.
\end{aligned} \tag{4.4}$$

Consequently, the denominator of (4.3) tends to 2 and the numerator is close to  $2[\text{Re}(z)y - \text{Im}(z)x]t$ , and so taking only the first term of Taylor series expansion (4.4) we obtain a simplified formula for asymmetry:

$$A_{CPT}(t) = \text{Slope} \cdot t + \text{Intercept} = [\text{Re}(z)y - \text{Im}(z)x]t + C. \tag{4.5}$$

In this context, it is natural to ask what are the values of  $x, y$ , for which neutral meson oscillations can be described by (4.3). The general rule is that for  $x, y (< 5\%)$  (3.12) can be reduced to a linear function (4.5). For  $D^0$  both  $x$  and  $y$  are less than 5% as demonstrated in Table.3.1. For this reason (4.5) can be successfully used for the approximate description of the neutral  $D$  meson oscillations.

## 4.5. Sensitivity tests for $|z| \leq 0.1$ used for data generation

In this section, I examine variability over the ensemble of pseudo-experiments of  $\delta \operatorname{Re}(z_{\text{fit}})$  and  $\delta \operatorname{Im}(z_{\text{fit}})$  with respect to the change of  $z$  used for generation. The examination was performed for two rather small statistics  $N = 10^5$  and  $N = 10^6$ . I plotted  $\delta \operatorname{Re}(z_{\text{fit}})$  and  $\delta \operatorname{Im}(z_{\text{fit}})$  against  $|z|$  and  $\Theta_{zz}$ . As we can see from Figure.4.4 the distributions of errors  $\delta \operatorname{Im}(z_{\text{fit}})$  and  $\delta \operatorname{Re}(z_{\text{fit}})$  over the ensemble of 100 pseudo experiments do not change with  $|z|$ . Moreover, Figure.4.4 indicates that both of the aforementioned parameters are invariant with respect to the change of argument  $\Theta_{zz}$  for the parameters from (4.1). Consequently, the sensitivity of testing CPTV for  $D^0$  seems to be related only to the number of decays in a pseudo-experiment. Similar reasoning can be repeated for a two parameter fit (Slope, Intercept) of simplified asymmetry model (4.5) to generated data. Figure.4.4 shows that the slope fit error is independent of the choice of parameter  $z$  within the examined range. The subscript of each slope denotes which component of complex parameter  $z$  was fixed. In addition, means of the pull distributions of fitted slopes are consistent with zero (see Figure.A.4, A.5), which suggests that there is no significant bias.

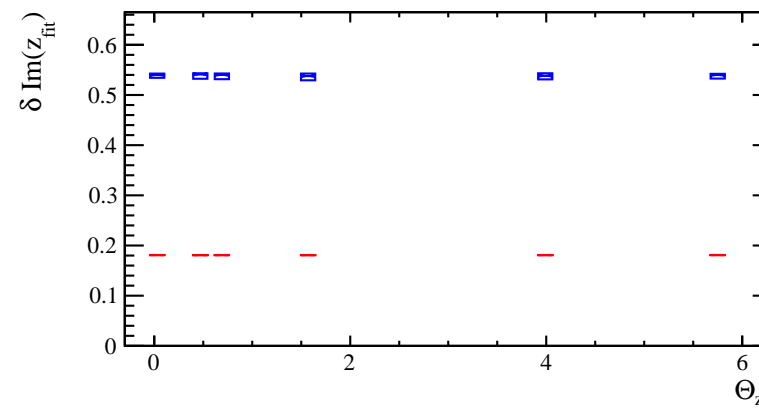
In the second chapter I mentioned that  $z \neq 0$  implies CPTV, which means that in order to measure CPTV we need to be capable of reliably measuring non-zero  $z$ . For low correlations between fitted parameters we can assess the limit of  $\delta z$  by using the exact differential method for propagation of errors. Which means that if I am fitting only one component of  $z$  each time, either  $\operatorname{Im}(z)$  or  $\operatorname{Re}(z)$ , then  $\delta z$  is equal to either  $\delta \operatorname{Im}(z)$  or  $\delta \operatorname{Re}(z)$ . Now let us make a simple observation that  $|z|$  is the upper boundary of  $|\operatorname{Im}(z)|$  and  $|\operatorname{Re}(z)|$  parameter values, which indicates that if we have no sensitivity for measuring  $|z| \neq 0$  we will have no sensitivity for  $\operatorname{Im}(z)$  and  $\operatorname{Re}(z)$ . The same rule can be applied to  $\operatorname{Slope}(z)$ , for which  $\operatorname{Slope}(z) \leq |z|y$  (4.5).

As expected, for  $10^5$  statistics, errors of all fitted parameters are roughly three times larger than for  $10^6$  decays per pseudo-experiment. As a result, the measured error values are all a few times larger than  $|z|$ . Promisingly, for  $10^6$  statistics, the fit error of  $\operatorname{Im}(z)$  oscillates around 0.18, whereas  $\delta \operatorname{Re}(z)$  is close 0.11. Similarly,  $\delta \operatorname{Slope}_{\operatorname{Im}}(z_{\text{fit}})$  revolves around  $7 \cdot 10^{-4}$ , which is only slightly above the slope value indicated by (4.5) for  $\Theta_{zz} = 0$ , namely  $\delta \operatorname{Slope}_{\operatorname{Im}}(z_{\text{fit}}) = \delta \operatorname{Re}(z_{\text{fit}})/y = 6.4 \cdot 10^{-4}$ .

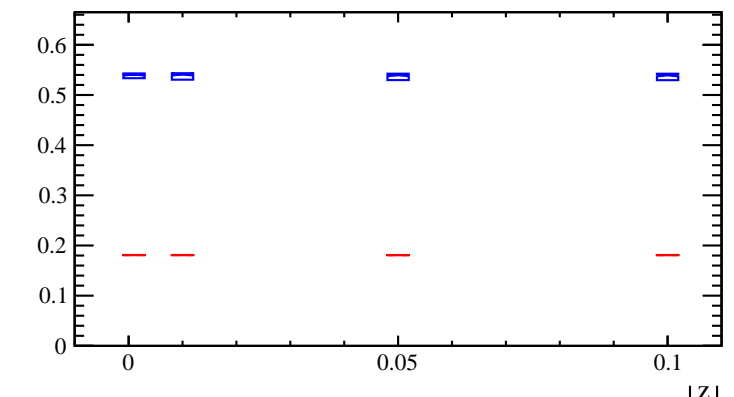
All things considered, we have no sensitivity<sup>4</sup> for CPTV since for  $10^5$   $\delta z$  was a few times larger than  $|z|$  and for  $10^6$  statistics  $|z| \approx \delta z$ .

---

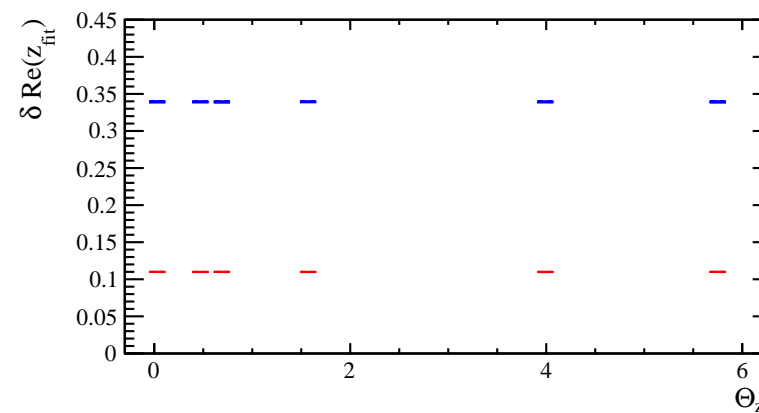
<sup>4</sup> Understood as 68% probability of  $z \neq 0$ .



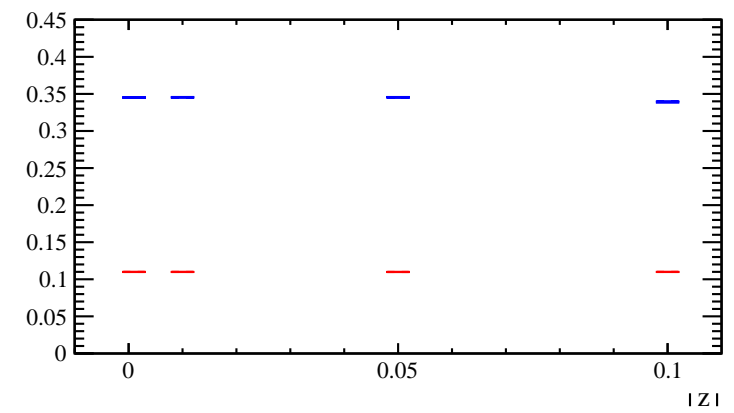
(a) data generated for  $|z| = 0.1$ ,  $\Theta_{zz} \in \{0, \frac{\pi}{8}, \frac{\pi}{4}, \frac{\pi}{2}, \frac{5\pi}{4}, \frac{9\pi}{5}\}$



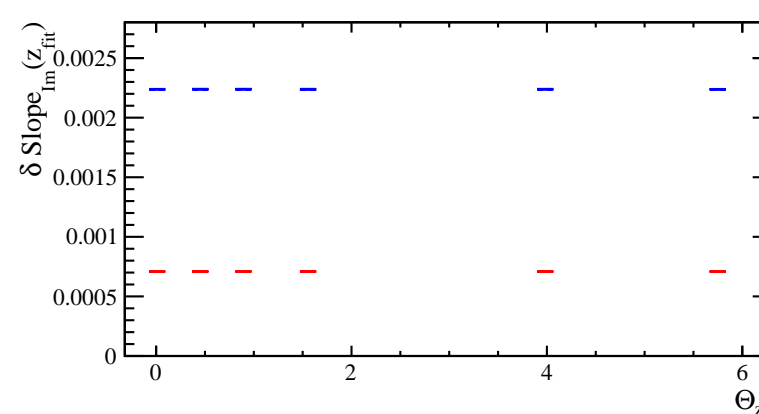
(b) data generated for  $|z| \in \{0.1, 0.05, 0.01, 0\}$ ,  $\Theta_{zz} = \frac{\pi}{4}$



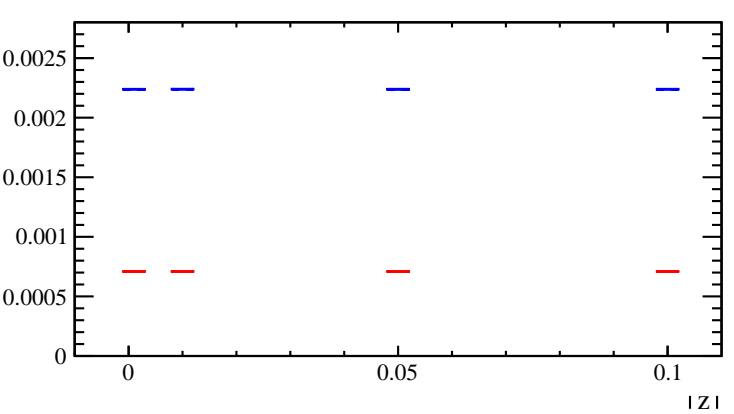
(c) data generated for  $|z| = 0.1$ ,  $\Theta_{zz} \in \{0, \frac{\pi}{8}, \frac{\pi}{4}, \frac{\pi}{2}, \frac{5\pi}{4}, \frac{9\pi}{5}\}$



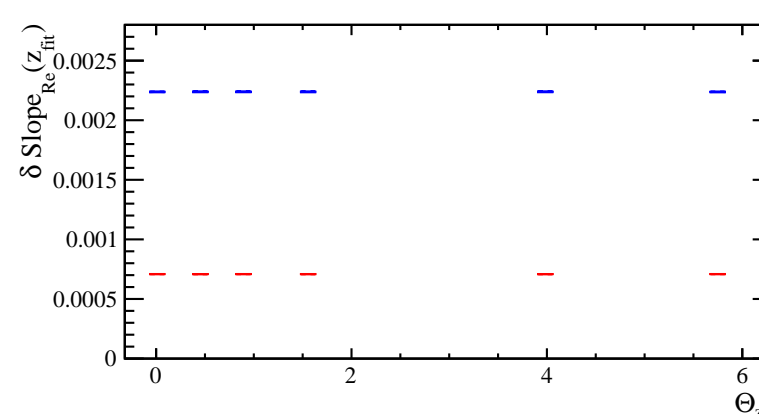
(d) data generated for  $|z| \in \{0.1, 0.05, 0.01, 0\}$ ,  $\Theta_{zz} = \frac{\pi}{4}$



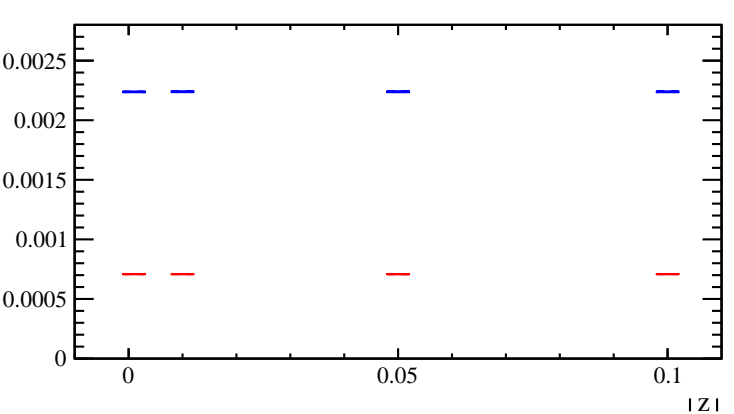
(e) data generated for  $|z| = 0.1$ ,  $\Theta_{zz} \in \{0, \frac{\pi}{8}, \frac{\pi}{4}, \frac{\pi}{2}, \frac{5\pi}{4}, \frac{9\pi}{5}\}$



(f) data generated for  $|z| \in \{0.1, 0.05, 0.01, 0\}$ ,  $\Theta_{zz} = \frac{\pi}{4}$

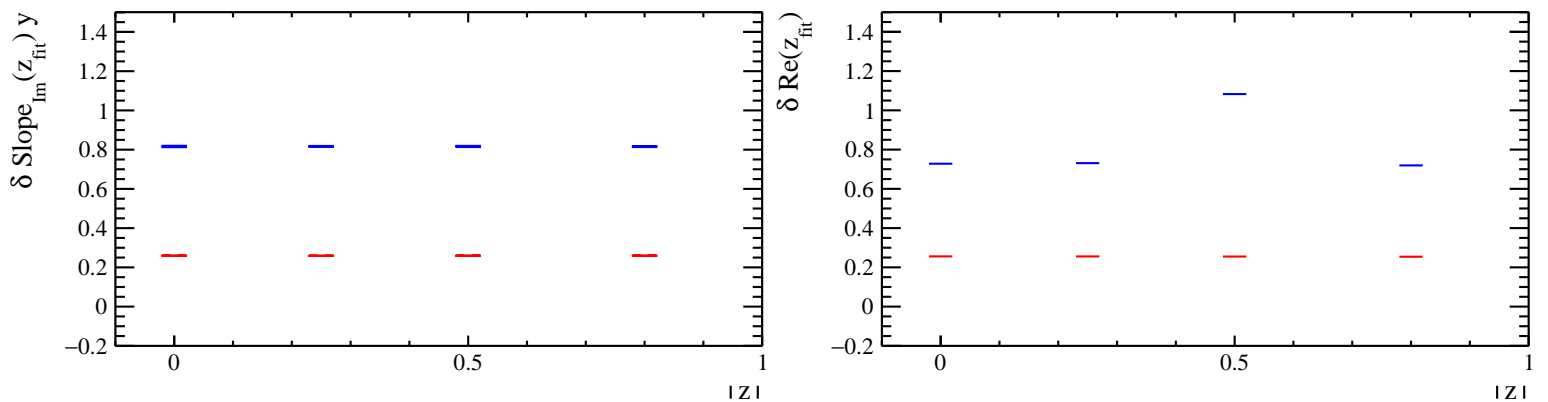


(g) data generated for  $|z| = 0.1$ ,  $\Theta_{zz} \in \{0, \frac{\pi}{8}, \frac{\pi}{4}, \frac{\pi}{2}, \frac{5\pi}{4}, \frac{9\pi}{5}\}$



(h) data generated for  $|z| \in \{0.1, 0.05, 0.01, 0\}$ ,  $\Theta_{zz} = \frac{\pi}{4}$

Figure 4.4 – Candle plots (boxes and medians displayed) of error distributions. Boxes are reduced to lines in this scale. The pseudo-experiments were performed for two different statistics  $10^5$  decays (blue),  $10^6$  decays (red). Candle plot bin widths set to  $10^{-7}$ . Subscript denotes the fixed component of  $z$ .



(a) Candle plot of  $\delta \text{Slope}_{\text{Im}}(z_{\text{fit}}) y$  distributions  
(boxes and medians displayed). Boxes reduced to lines in this scale.

(b) Candle plot of  $\delta \text{Re}(z_{\text{fit}})$  distributions  
(only medians displayed).

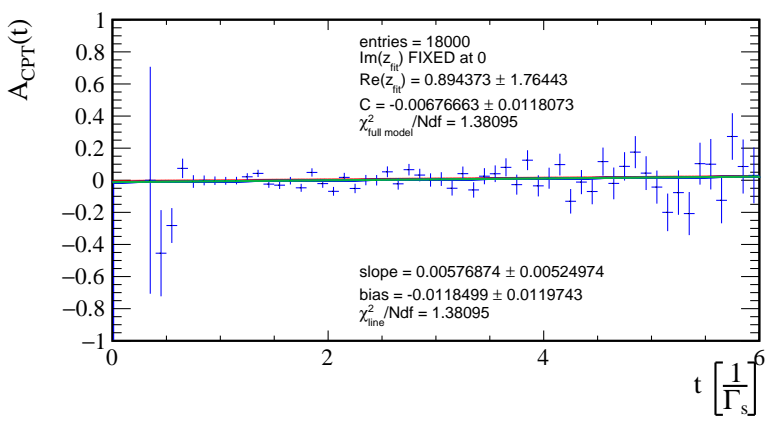
Figure 4.5 – Red- $1.8 \cdot 10^5$  statistics, blue- $1.8 \cdot 10^4$  statistics. Parameters used for data generation  $|z| \in \{0, 0.25, 0.5, 0.8\}$ ,  $\Theta_{zz} = 0$ . 100 pseudo-experiments per candle. Candle plot bin widths  $10^{-7}$ . Subscript Im means that  $\text{Im}(z)$  was fixed at 0 during fit.

## 4.6. Sensitivity tests for $|z| \leq 0.8$ used for data generation

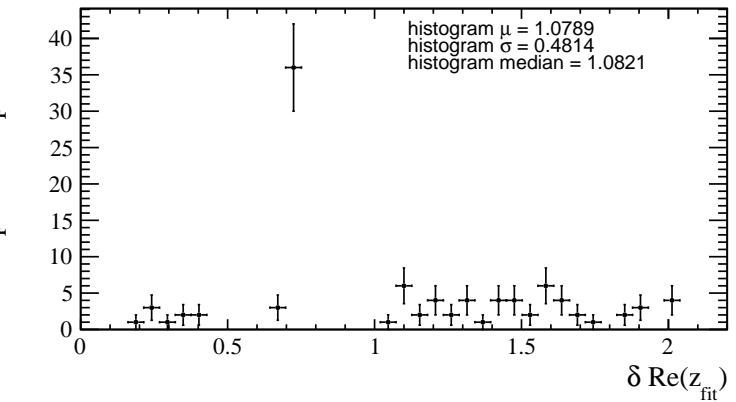
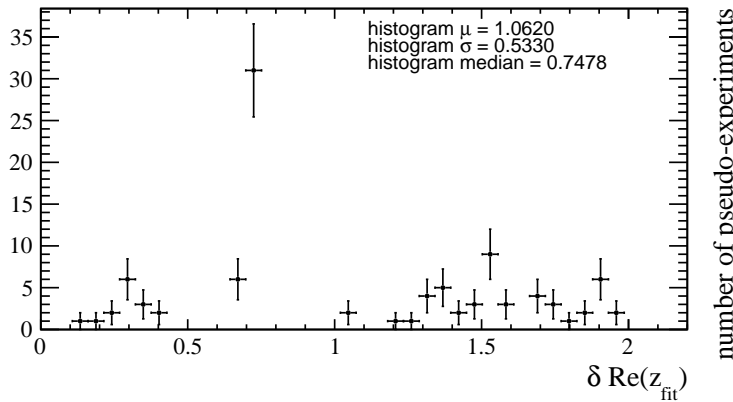
From the previous section we already know that we have no sensitivity for testing CPTV when  $|z| = 0.1$  for  $10^6$  and  $10^5$  statistics. However, this observation does not necessarily need to hold for much greater  $|z| = 0.8$  (used for data generation) and low statistics  $1.8 \cdot 10^4$ . In this section, I demonstrate the findings of a fitting procedure analogous to that showed in the previous section. I generated asymmetry dataset for  $|z| = 0.8$ ,  $\Theta_{zz} = 0$  ( $\text{Re}(z) = 0.8$ ,  $\text{Im}(z) = 0$ ) parameters. This time I fitted only one component of  $z$  in each pseudo-experiment  $\text{Re}(z)$ . The imaginary part was fixed at zero. Fits were performed for 200 sets of generated asymmetry datasets, more specifically 100 pseudo-experiments with  $1.8 \cdot 10^4$  decays each<sup>5</sup>, as well as, 100 pseudo-experiments with ten times larger statistics. According to [21] the FOCUS collaboration measured the upper limit of CPTV at the level of  $O(1)$ <sup>6</sup>. From 100 fits of both (3.12) and (4.5) to MC generated data, I established that the fit errors are statistically of the same order of magnitude as the one presented by the FOCUS collaboration (see Figures 4.6, 4.5, A.9). However the obtained results are consistent with zero, therefore no sensitivity, even for  $|z| = 0.8$ , can be assessed. In addition, I compared the obtained medians of  $\delta \text{Slope}_{\text{Im}}(z_{\text{fit}})$  distributions, with the corresponding medians of  $\delta \text{Re}(z_{\text{fit}})$  distributions acquired from 100 fits of the real component of  $z$  (see Figure 4.5). The obtained medians are pretty close in spite of the considerably low statistics. However in the case of  $1.8 \cdot 10^4$  MC events per pseudo-experiment, there is a significant number of fits which errors are quite far from each histogram's mean and median (see Figure 4.7). This is the reason why this time, unlike for the rest of error distribution plots, I did not draw candle plot boxes (see chapter 1 section Candle plots). The medians of pull distributions of the fitted parameters are consistent with zero to within 10% of the each pulls' standard deviation (see Appendix Figure A.9), which shows that there is no significant bias.

<sup>5</sup>  $1.8 \cdot 10^4$  of  $D^0 \rightarrow f$  decays and  $1.8 \cdot 10^4$  of  $\bar{D}^0 \rightarrow \bar{f}$  decays.

<sup>6</sup>  $\text{Re}(z) = 0.83 \pm 0.65$ .



number of pseudo-experiments



number of pseudo-experiments

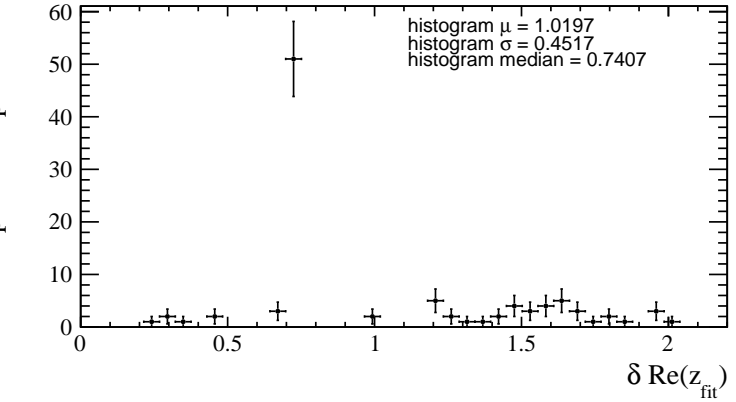
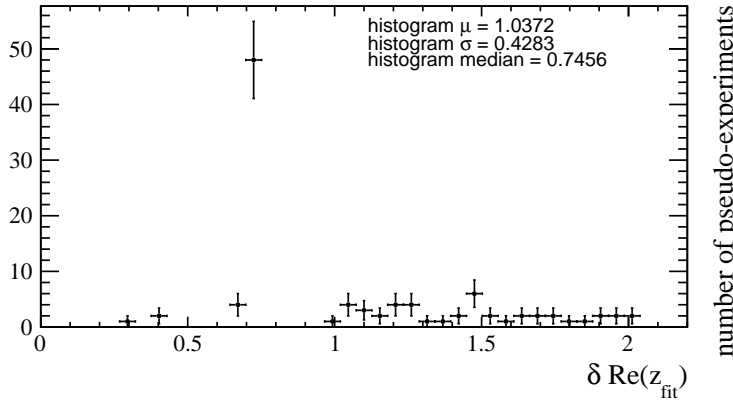
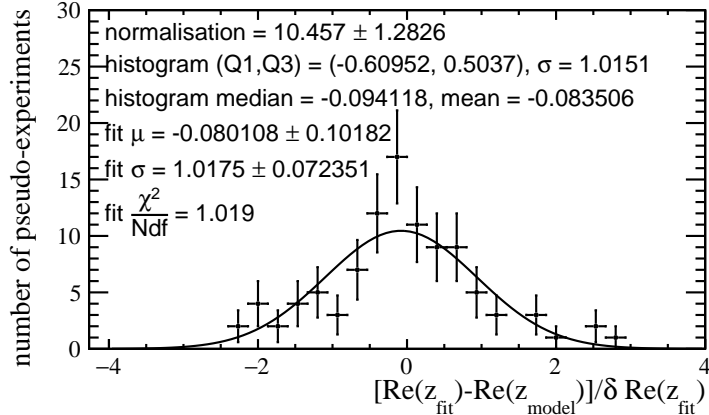
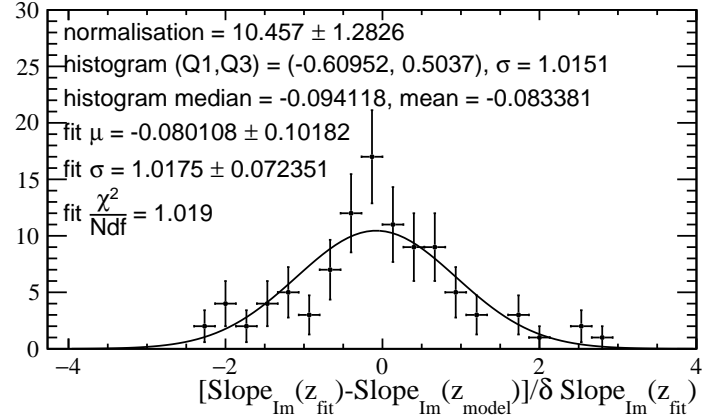


Figure 4.7 – Histograms of  $\delta \text{Re}(z_{\text{fit}})$  distributions.  $\text{Im}(z)$  was fixed at 0 during fit. For each of these histograms there is a significant number of fits, which errors are quite far from the histogram mean and median. Bin widths set to 0.05.

## 4.7. Sensitivity tests for $|z| = 0.1$ used for generation of $6.5 \cdot 10^7$ decays



(a)  $\text{Re}(z)$  pull distribution for  $6.5 \cdot 10^7$  statistics,  
data was generated for  $|z| = 0.1$ ,  $\Theta_{zz} = 0$ ,  
 $\text{Im}(z)$  was fixed at 0 during fit. Bin width set to 0.013.



(b)  $\text{Slope}_{\text{Im}}(z)$  pull distribution for  $6.5 \cdot 10^7$  statistics,  
data was generated for  $|z| = 0.1$ ,  $\Theta_{zz} = 0$ ,  
 $\text{Im}(z)$  was fixed at 0 during fit. Bin width set to 0.013.

Figure 4.8

In the previous two sections, I established that for  $D^0$  the values of the CPTV parameter components ( $\text{Im}(z)$ ,  $\text{Re}(z)$ ) are independent of  $|z|$  and  $\Theta_{zz}$ . In view of that, it is natural to conclude that the available statistics is the main parameter controlling both means and medians of the fit error distributions. In this context, we should have a full freedom of choosing the value of the CPTV parameter used for generation of data utilised in the assessment of the aforementioned level of sensitivity. In practice, however this conclusion might be false. The full examination of the sensitivity level in  $D^0$  system would require many different values of  $z$  for data generation. In this thesis, I restricted myself only to the first step of such analysis. Namely I generated 100 pseudo-experiments for a single  $z$  ( $|z| = 0.1$ ,  $\Theta_{zz} = 0$ ). Just as in the previous section, the imaginary part was fixed at zero. The result of these pseudo-experiments can be found in Figure 4.8, 4.9 and the exemplary fit of asymmetry can be found in Figure 4.11.

From Figure 4.9 we can assess that  $z$  of order 0.1 can be measured at the level of sensitivity of 7 standard deviations,  $|z|/\delta z \approx 7$  (where  $\delta z \approx 0.014$  see Figure 4.9). In the light of the supposed independence of  $\delta z$  distribution with regards to the choice of  $|z|$  and  $\Theta_{zz}$ , discussed in the previous two sections, we should expect to be able to measure  $z$  of order  $O(10^{-2})$  at the level of sensitivity of one standard deviation. Therefore the next step of the analysis should be to generate 100 pseudo-experiments for  $|z| = 0.01$ ,  $\Theta_{zz} = 0$  and verify this hypothesis. Full studies of the level of sensitivity of testing CPTV for  $6.5 \cdot 10^7$  would require many more pseudo-experiments generated for different  $z$  parameters from the range  $|z| < 1$ ,  $\Theta_{zz} \in [0, 2\pi]$ .

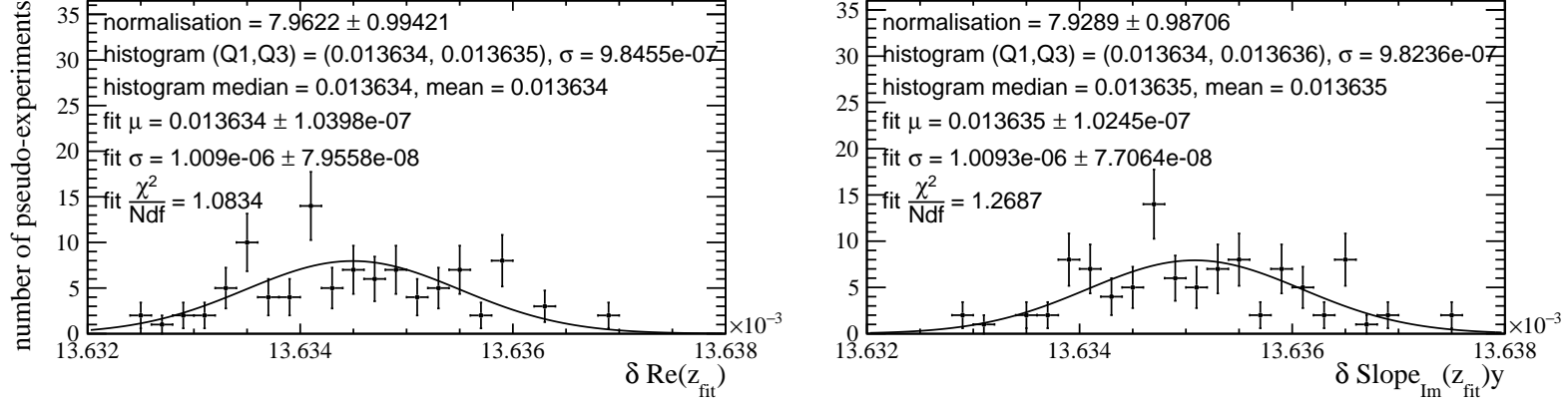
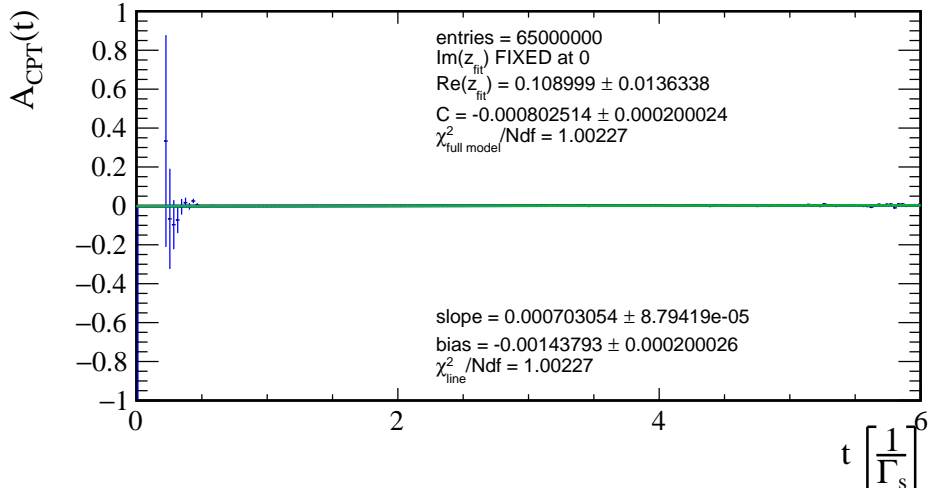
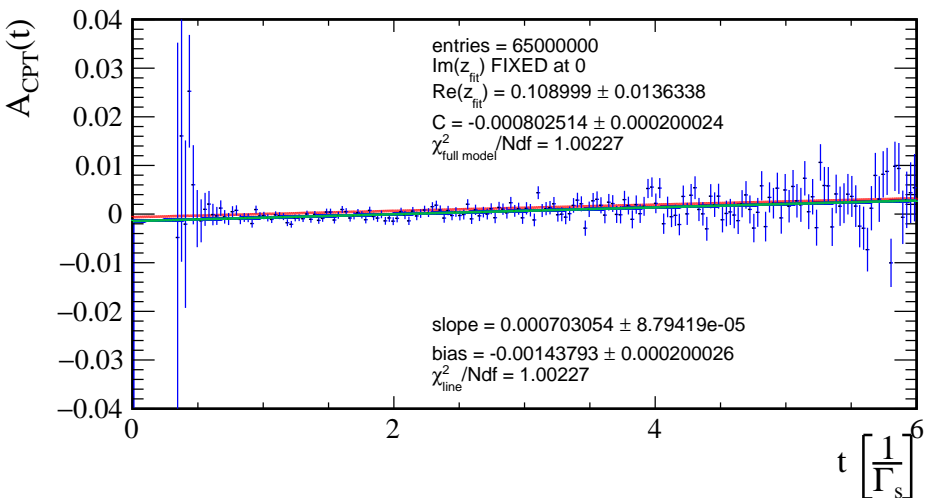


Figure 4.9



(a) Exemplary fit full range of  $A_{CPT}(t)$  values.



(b) Exemplary fit zoomed in version of (a).

Figure 4.10 – Exemplary fit from amongst 100 fits of asymmetry to MC generated data, where  $|z| = 0.1$ ,  $\Theta_{zz} = 0$  ( $\text{Re}(z) = 0.1$ ,  $\text{Im}(z) = 0$ ) were used for generation. Bin width set to 0.03. Green - simplified asymmetry (4.5), blue - full asymmetry fit (3.12), red - asymmetry model (3.12) with parameters from (4.1). Blue points with error bars represent the generated asymmetry dataset histogram. Fit results and the plotted model are overlapping and so not all of them are visible.

## 5. Summary

In the 1st and 2nd chapter, I presented the basic theoretical concepts from the area of neutral meson oscillations and introduced a formalism used to create the MC generator presented in the 3rd chapter. The developed meson decay generator is very general and can be used to simulate neutral meson decays in many different channels. Throughout the last two chapters I established that, for the studied CPTV parameters used for asymmetry dataset generation, the available statistics is the main parameter controlling the magnitude of the fit error of CPTV parameter  $z$ . I also determined that N-fold decrease of statistics results in  $\frac{1}{\sqrt{N}}$  change of the magnitude of fit errors, as expected. More specifically, for both  $D^0$  and  $M_s^0$  (see sections 3.04, 4.04, 4.05) a tenfold increase in statistics causes a roughly threefold ( $\sqrt{10} \approx 3$ ) decrease of the  $z$  component errors. Remarkably, for  $6.5 \cdot 10^7$  statistics (see section 4.7) corresponding to the number of entries in  $D^0 \rightarrow K^- \pi^+$  decay mode from LHCb Run 1 (2011-2012), we observe that the errors shrink by the factor of  $\frac{1}{8}$ , which is close to  $\frac{1}{\sqrt{65}}$ .

In the 3rd chapter, I generated asymmetry data for a fictitious meson  $M_s^0$  so as to simulate 100 meson decays. Subsequently, I examined the dependence of 100 asymmetry model (3.11) fits to MC generated data on the value of CPTV parameter  $z$  used for data generation. We can observe that the medians of  $\delta \text{Re}(z_{\text{fit}})$  and  $\delta \text{Im}(z_{\text{fit}})$  distributions oscillate within a certain finite range (see Figures.3.7.a, 3.8.a), which might be the result of high correlations between fitted parameters. In the observed case the dependence of the aforementioned error distributions on  $|z|$  is very weak and further studies are needed to fully determine its scale.

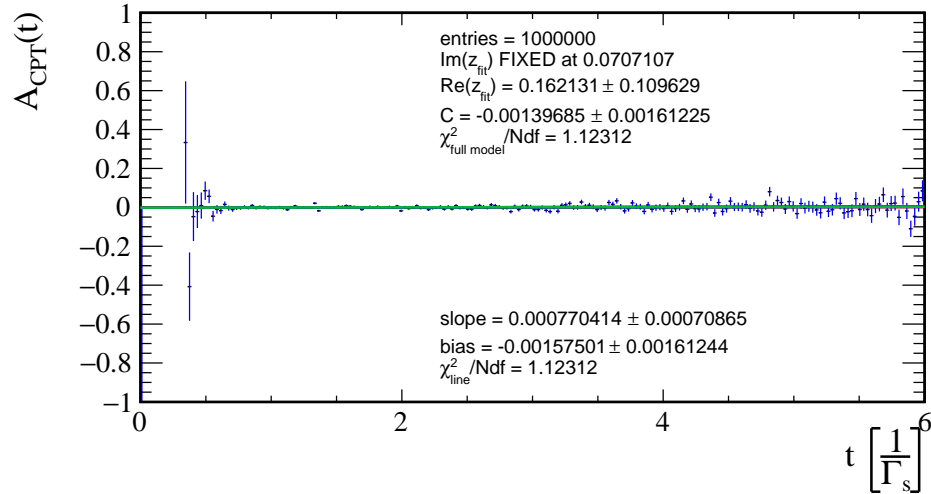
In the case of meson  $D^0$  I performed tests for  $10^6$ ,  $10^5$  where  $|z| < 0.1$ ,  $\Theta_{zz} = \frac{\pi}{4}$  were used for MC events generation. Moreover I analysed pseudo-experiments, for which  $|z| < 0.8$ ,  $\Theta_{zz} = 0$  for  $1.8 \cdot 10^4$  and  $1.8 \cdot 10^5$  generated decays. For  $1.8 \cdot 10^4$  statistics I obtained very mild sensitivity of one sigma of measuring CPTV parameter  $z$ , which is in agreement with the result obtained by the FOCUS collaboration [21]. Finally, I determined that the sensitivity of measuring  $z = 0.1$  for  $6.5 \cdot 10^7$  statistics is at the level of 7 standard deviations. For this statistics, I performed 100 pseudo-experiments, where  $|z| = 0.1$  and  $\Theta_{zz} = 0$  were used for generation of decays. The full examination of the sensitivity of measuring  $z$  for the statistics from the LHCb Run 1 (2011-2012)  $D^0 \rightarrow K^- \pi^+$  decay mode, would require many more pseudo-experiments generated for different  $z$  parameters from the range  $|z| < 1$ ,  $\Theta_{zz} \in [0, 2\pi]$ . We should put special emphasis on the region of  $z = 0.01$ , which is of the same order of magnitude as the error obtained for  $6.5 \cdot 10^7$  statistics in section 4.7.

In this thesis, I limited myself to using my MC generator for low statistics. In the future, I plan to test the level of sensitivity for CPTV for much larger statistics. Most notably for the statistics of  $1.5 \cdot 10^8$ , which is available for the LHCb Run 2 (2015-2018)  $D^0 \rightarrow K^- \pi^+$  decay mode, as well as for data from the LHCb Run 3, which is expected to reach  $10^9$  events in this channel.

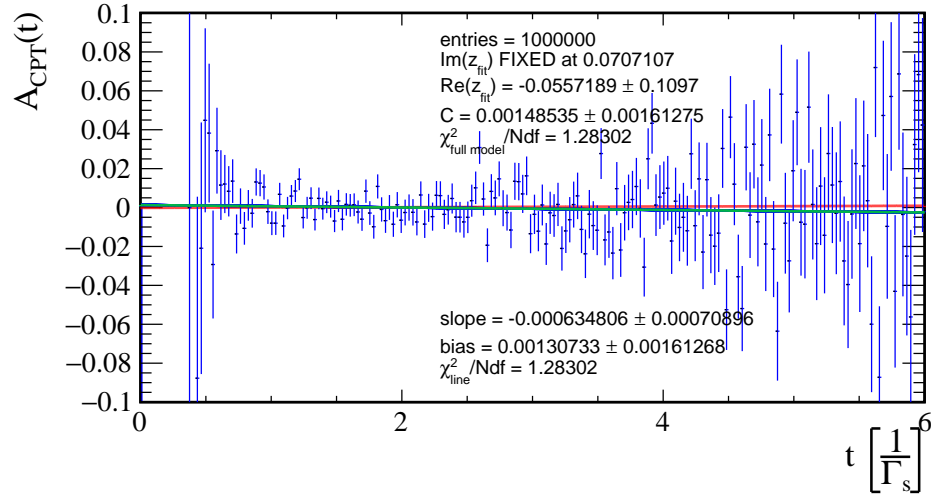
# Bibliography

- [1] Mark Thomson. Modern particle physics. *Cambridge University Press*, ISBN 978-1-107-03426-6:1–28, 2013.
- [2] A.D. Sakharov. Violation of CP Invariance, C Asymmetry, and Baryon Asymmetry of the Universe. *Pisma Zh. Eksp. Teor. Fiz.*, 5:32–35, 1996.
- [3] G Lüders. On the equivalence of invariance under time reversal and under particle-antiparticle conjugation for relativistic field theories. *Dan. Mat. Fys. Medd.*, 28(5):1–17, 1954.
- [4] W. Pauli. Exclusion Principle, Lorentz Group and Reflection of Space-Time and Charge.:In Niels Bohr and the Development of Physics, ed. by W. Pauli (Pergamon Press, New York 1955, 30–51).
- [5] R. Jost. Eine Bemerkung zum CPT-Theorem. *Hel. Phys. Acta*, 30:409–416, 1957.
- [6] O.W. Greenberg. CPT violation implies violation of CPT invariance. *Phys. Rev. Lett. D*, 89.
- [7] V.A Kostelecky. CPT, T, and Lorentz Violation in Neutral-Meson Oscillations. *Phys. Rev. D*, 64, 2001.
- [8] V.A.Kostelecky B.R. Edwards. Searching for CPT Violation with Neutral-Meson Oscillations.
- [9] M. Tanabashi et al. (Particle Data Group). CP Violation in the Quark Sector. *Phys. Rev. D*, 98:030001, (2018) update 2019.
- [10] M.S.Sozzi. Discrete Symmetries and CP Violation From Experiment to Theory. *Oxford University Press*, ISBN 978–0–19–929666–8:276–380, 2008.
- [11] V. Weisskopf and E. P. Wigner. *Z. Phys.* 63, 54 (1930); *Z. Phys.* 65, 18 (1930).
- [12] Academic Press (1968). Appendix A of P.K. Kabir, The CP Puzzle: Strange Decays of the Neutral Kaon.
- [13] M. Tanabashi et al. (Particle Data Group). *Phys. Rev. D*.
- [14] John W. Tukey. Exploratory Data Analysis. *Addison-Wesley*, 1977.
- [15] ROOT.6.20 reference guide THistPainter, TH1::GetMean(), TH1::GetMedian.
- [16] C. Patrignani et al. (Particle Data Group). *Chin. Phys. C*, 40:100001, 2016.
- [17] LHCb@InternationalMasterclasses Measuring the D0 lifetime at the LHCb.  
<https://lhcb-public.web.cern.ch/en/LHCb-outreach/masterclasses/en/D0Lifetime.html>.
- [18] P. Lebrun S. Myers R. Ostojic J. Poole P. Proudlock O. Bruning, P. Collier. LHC Design Report, The LHC Main, Ring. *CERN*, 92–9083-224 0.
- [19] LHCb collaboration. The LHCb detector. <http://lhcb-public.web.cern.ch/en/Detector/Detector-en.html>.
- [20] LHCb collaboration. Updated measurement of time-dependent CP-violating observables in  $B_s^0 \rightarrow J/\psi K^+ K^-$  decays. *Eur. Phys. J. C* 79 (2019) 706, LHCb-PAPER-2019-013; CERN-EP-2019-108.
- [21] et al J. M. Link. Charm System Tests of CPT and Lorentz Invariance with FOCUS. *Phys.Lett.B*, 556:7–13, 2003.

## A. Appendix

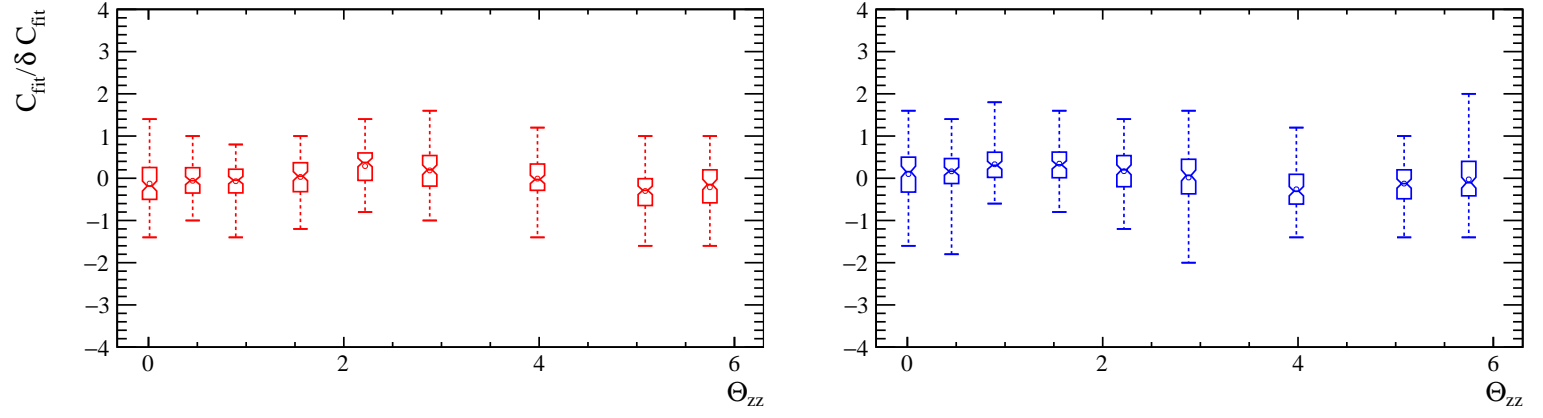


(a) Exemplary fit full range of  $A_{CPT}(t)$  values.



(b) Exemplary fit, zoomed in version of (a).

Figure A.1 – Exemplary fit from amongst 100 fits of asymmetry to MC generated data, where  $|z| = 0.1$ ,  $\Theta_{zz} = \frac{\pi}{4}$  ( $\text{Re}(z) \approx 0.0707$ ,  $\text{Im}(z) \approx 0.0707$ ) were used for generation. Bin width set to 0.03. Green - simplified asymmetry (4.5), blue - full asymmetry (3.12) fit, red - asymmetry model (3.12) with parameters from (4.1). Blue points with error bars represent the generated asymmetry dataset. Fit results and the plotted model are overlapping and so not all of them are visible.



(a) Candle plot  $C$  parameter pull distribution for  $10^6$  entries

(b) Candle plot  $C$  parameter pull distribution for  $10^5$  entries

Figure A.2 – Candle plots of  $C$  parameter pull distributions for  $M_s^0$  (all six markers displayed). Candle plot bin widths set to  $10^{-6}$ .

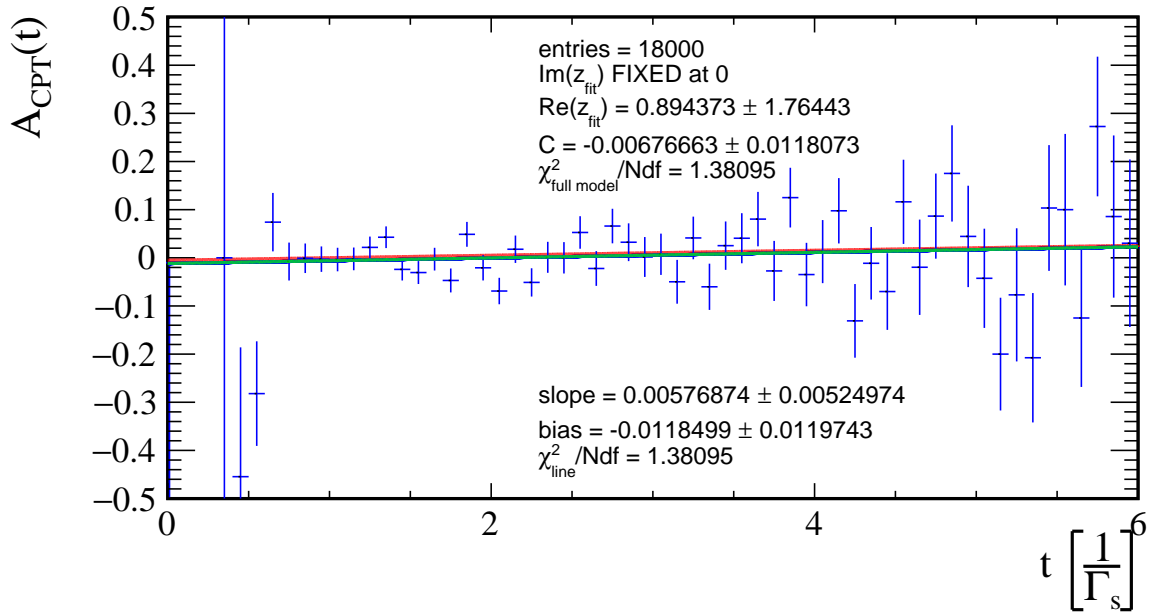
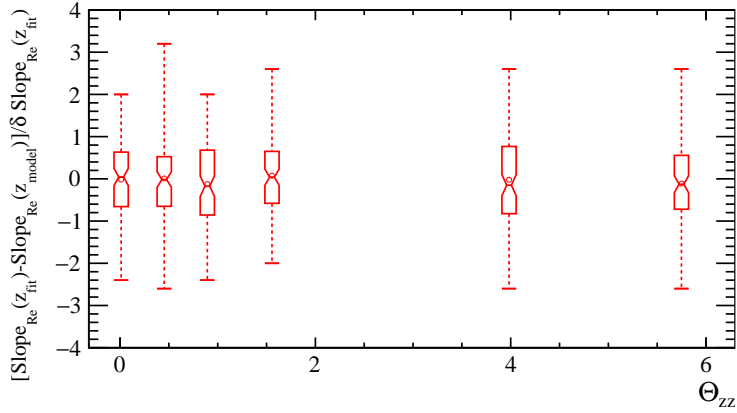
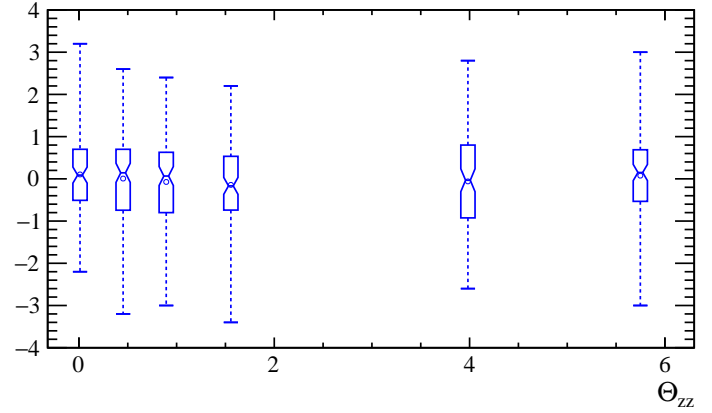


Figure A.3 – Exemplary, zoomed in version of fit from amongst 100 fits of asymmetry to MC generated data, where  $|z| = 0.8$ ,  $\Theta_{zz} = 0$  ( $\text{Re}(z) = 0.8$ ,  $\text{Im}(z) = 0$ ) were used for generation. Exemplary fit for full range of  $A_{CPT}(t)$  can be found in Figure 4.6. Bin width set to 0.1. Green - simplified asymmetry (4.5), blue - full asymmetry (3.12) fit, red - asymmetry model (3.12) with parameters from (4.1). Blue points with error bars represent the generated asymmetry dataset. Fit results and the plotted model are overlapping and so not all of them are visible.

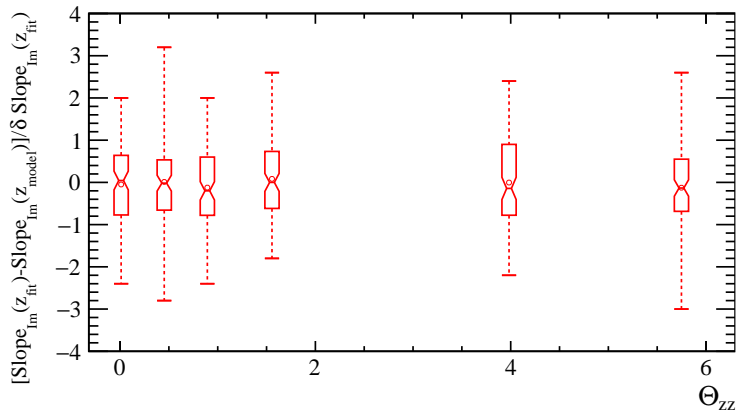


(a)  $10^6$  decays

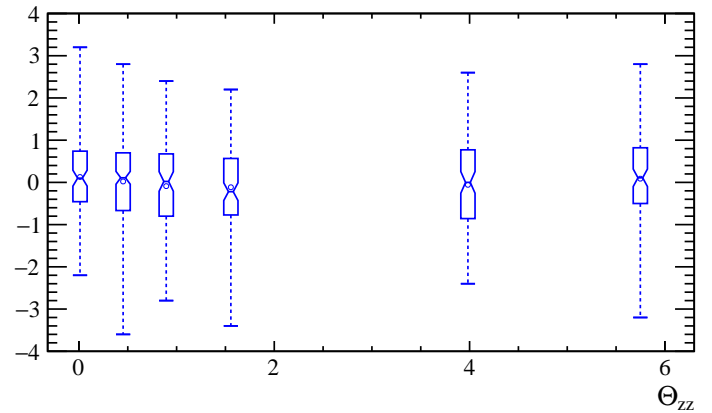


(b)  $10^5$  decays

Figure A.4 –  $10^5$  decays blue line,  $10^6$  decays red line. Candle plot  $\text{Slope}_{\text{Re}}(z)$  pull distributions for  $D^0$  (all six markers displayed), generated for parameter  $z$ , are defined under each plot, candle plot bin widths set to  $10^{-7}$ . Subscript Re means that  $\text{Re}(z)$  was fixed during fit.

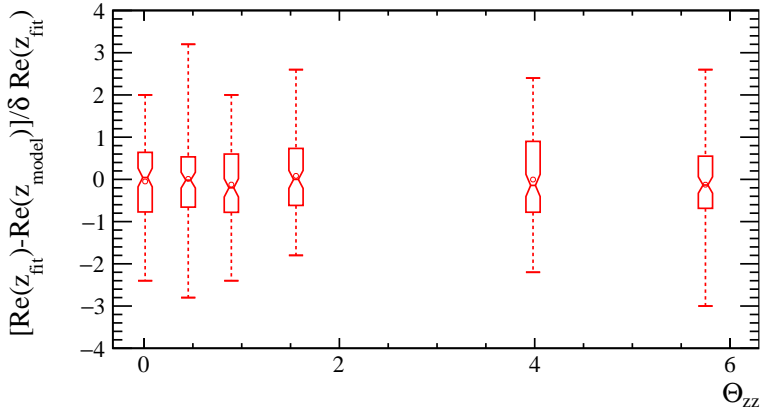


(a)  $10^6$  decays

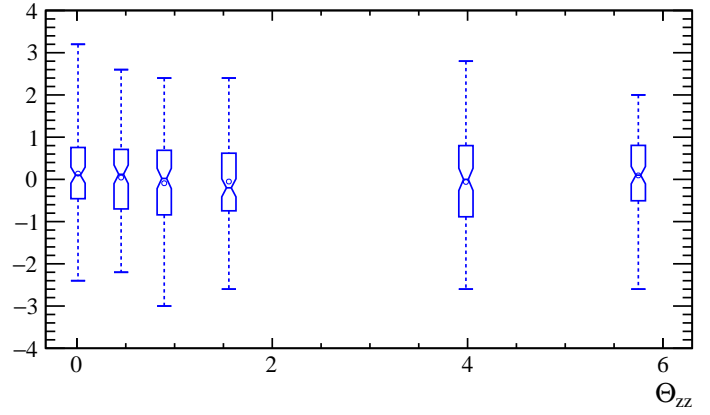


(b)  $10^5$  decay

Figure A.5 –  $10^5$  decays blue line,  $10^6$  decays red line. Candle plot  $\text{Slope}_{\text{Im}}(z)$  pull distributions for  $D^0$  (all six markers displayed), generated for parameter  $z$ , are defined under each plot, candle plot bin widths set to  $10^{-7}$ . Subscript Im means that  $\text{Im}(z)$  was fixed during fit.

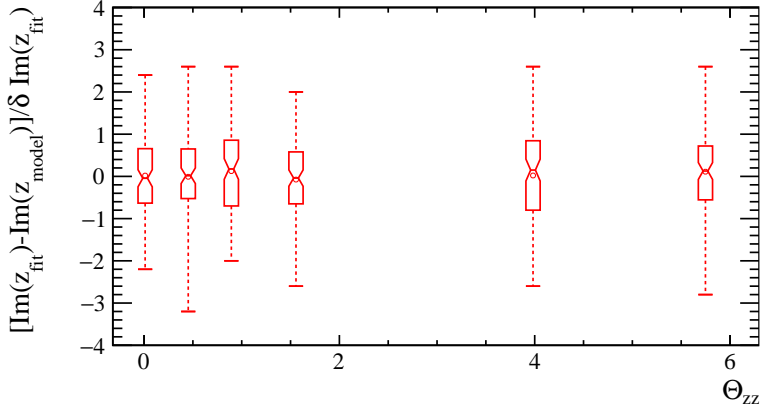


(a)  $|z| = 0.1, \Theta_{zz} \in \{0, \frac{\pi}{8}, \frac{\pi}{4}, \frac{\pi}{2}, \frac{5\pi}{4}, \frac{9\pi}{5}\}$

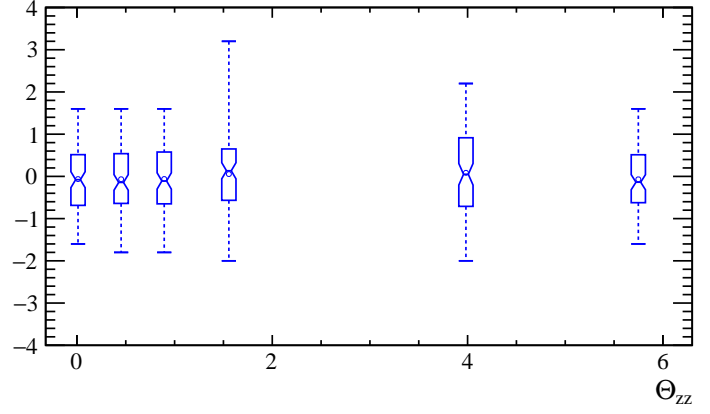


(b)  $|z| = 0.1, \Theta_{zz} \in \{0, \frac{\pi}{8}, \frac{\pi}{4}, \frac{\pi}{2}, \frac{5\pi}{4}, \frac{9\pi}{5}\}$

Figure A.6 –  $10^5$  decays blue line,  $10^6$  decays red line. Candle plot  $\text{Re}(z)$  pull distributions for  $D^0$  (all six markers displayed), candle plot bin widths set to  $10^{-7}$ .  $\text{Im}(z)$  was fixed during fit.

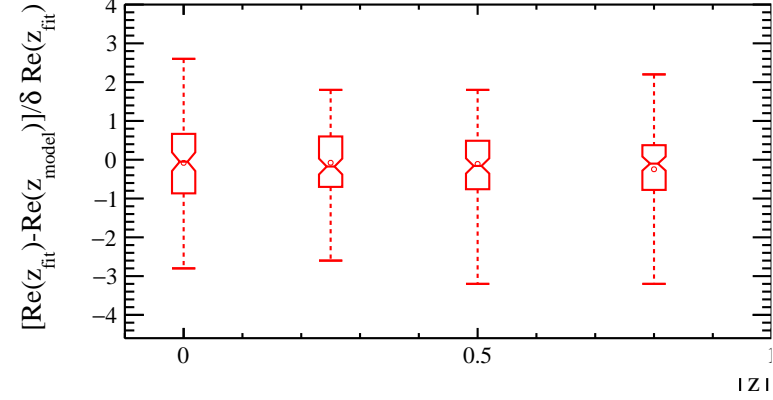


(a)  $|z| = 0.1, \Theta_{zz} \in \{0, \frac{\pi}{8}, \frac{\pi}{4}, \frac{\pi}{2}, \frac{5\pi}{4}, \frac{9\pi}{5}\}$

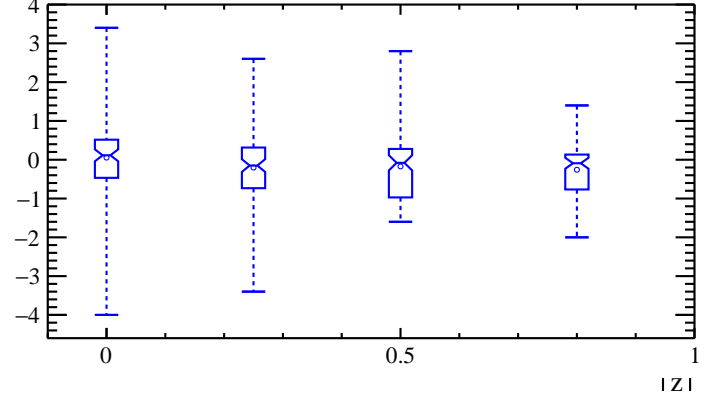


(b)  $|z| = 0.1, \Theta_{zz} \in \{0, \frac{\pi}{8}, \frac{\pi}{4}, \frac{\pi}{2}, \frac{5\pi}{4}, \frac{9\pi}{5}\}$

Figure A.7 –  $10^5$  decays blue line,  $10^6$  decays red line. Candle plot  $\text{Im}(z)$  pull distributions for  $D^0$  (all six markers displayed), candle plot bin widths set to  $10^{-7}$ .  $\text{Re}(z)$  was fixed during fit.

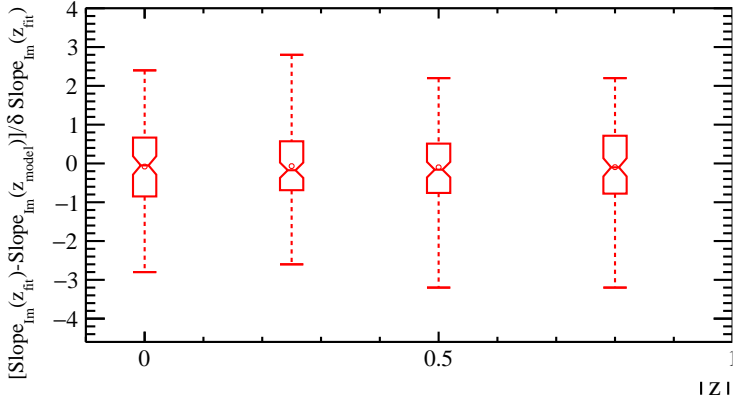


(a)  $|z| \in \{0, 0.25, 0.5, 0.8\}$ ,  $\Theta_{zz} = 0$

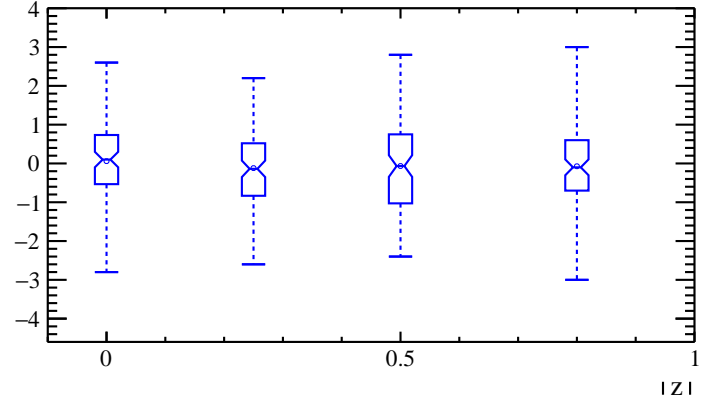


(b)  $|z| \in \{0, 0.25, 0.5, 0.8\}$ ,  $\Theta_{zz} = 0$

Figure A.8 –  $1.8 \cdot 10^4$  decays blue line,  $1.8 \cdot 10^5$  decays red line. Candle plot  $\text{Re}(z)$  pull distributions for  $D^0$  (all six markers displayed). Data generated for parameter  $z$  values defined under each plot. Candle plot bin widths set to  $10^{-7}$ .  $\text{Im}(z)$  was fixed during fit.



(a)  $|z| \in \{0, 0.25, 0.5, 0.8\}$ ,  $\Theta_{zz} = 0$



(b)  $|z| \in \{0, 0.25, 0.5, 0.8\}$ ,  $\Theta_{zz} = 0$

Figure A.9 –  $1.8 \cdot 10^4$  decays blue line,  $1.8 \cdot 10^5$  decays red line. Candle plot  $\text{Slope}_{\text{Im}}(z)y$  pull distributions for  $D^0$  (all six markers displayed). Data generated for parameter  $z$  values defined under each plot. Candle plot bin widths set to  $10^{-7}$ . Subscript Im means that  $\text{Im}(z)$  was fixed during fit.